



Wide-ranging survey on the laminar flow of individual Taylor bubbles rising through stagnant Newtonian liquids

J.D.P. Araújo, J.M. Miranda, A.M.F.R. Pinto, J.B.L.M. Campos *

Centro de Estudos de Fenómenos de Transporte, Departamento de Engenharia Química, Universidade do Porto, Faculdade de Engenharia, Rua Dr. Roberto Frias, 4200-465 Porto, Portugal

ARTICLE INFO

Article history:

Received 1 November 2011

Received in revised form 3 February 2012

Accepted 13 March 2012

Available online 23 March 2012

Keywords:

Slug flow

Numerical simulation

Ansys FLUENT

Taylor bubble velocity

Taylor bubble shape

Flow field around bubble

ABSTRACT

A wide-ranging numerical survey of the rising of individual Taylor bubbles through vertical columns of stagnant Newtonian liquid in laminar flow regime is presented in the present paper. The CFD procedure applied is based in the volume of fluid (VOF) methodology of the commercial package Ansys FLUENT. The simulations performed covered wide ranges of column diameters and viscosities, corresponding to Morton and Eötvös numbers within the intervals of 4.72×10^{-5} to 104 and 6–900, respectively. Several relevant hydrodynamic features regarding the three main flow regions considered (nose region, liquid film and wake region) were determined. In some cases, these features were favourably compared to predictions of available correlations and theoretical equations. Due to the lack of published material about the wake structure, a particular interest was taken on this flow region, where some general equations are presented to estimate the related hydrodynamic features. This study can become a useful tool for future studies on slug flow systems.

© 2012 Elsevier Ltd. All rights reserved.

1. Introduction

A variety of two-phase flow patterns can happen when gas and liquid flow simultaneously in a vertical tube. Over a wide range of flow rates, there is the formation of a flow pattern consisting on a pseudo-periodic appearance of long bullet-shaped bubbles, frequently called Taylor bubbles, which occupy most of the available cross section of the channel. These bubbles are separated from the wall by a thin liquid film that expands when it reaches the trailing edge of the bubble, inducing the formation of a liquid wake. The bubbles are separated by liquid plugs flowing co-currently.

The gas–liquid flow pattern described above is commonly known as slug flow, and has a huge industrial relevance, due to its numerous applications related to heat and mass transfer process units, transportation of hydrocarbon pipelines, geological studies and nowadays even in the exponential growing field of microflow systems (Fabre and Liné, 1992; Mercier et al., 1997; Ghosh and Cui, 1999; Branger et al., 2001; Taha and Cui, 2002; Chung et al., 2007; Angeli and Gavrilidis, 2008; Pangarkar et al., 2008).

The problem concerning the hydrodynamic characteristics of vertical slug flow is governed by the interaction between gravitational, interfacial, viscous and inertial forces. Performing a dimensional analysis based on the Pi-Buckingham theorem, and

neglecting the viscosity and inertial forces in the gas, the referred problem can be reduced to three dimensionless groups:

- Eötvös number, $Eo = g(\rho_L - \rho_G)D^2/\sigma$, which represents the ratio of surface tension and gravitational effects.
- Morton number, $M = g\mu_L^4(\rho_L - \rho_G)/\rho_L^2\sigma^3$, also called the property group since it only contains the properties of the fluid.
- Froude number, $Fr = U_{TB}/\sqrt{gD(\rho_L - \rho_G)/\rho_L}$, which defines the ratio of inertial and gravitational forces.

where ρ_L and ρ_G are the liquid and gas densities, respectively, D the tube diameter, σ the surface tension, μ_L the dynamic viscosity of the liquid, and U_{TB} the Taylor bubble velocity.

Other important dimensionless numbers can be derived, such as the inverse viscosity number, $N_f = \rho_L\sqrt{gD^3}/\mu_L = (Eo^3/M)^{1/4}$, and the Archimedes number, obtained from manipulation of N_f ($Ar = N_f^2$).

Since the early 1940s, a substantial amount of research has been devoted to understand the principles of slug flow. Dumitrescu (1943) studied the rise of a single Taylor bubble through stagnant liquid in a tube, based on the potential flow theory, and concluded that the bubble rising velocity should be given by:

$$U_{TB} = 0.351\sqrt{gD} \quad (1)$$

Some years later, Davies and Taylor (1950) generally agreed with this equation but estimated a constant of 0.328 instead of 0.351. White and Beardmore (1962) carried out an extensive

* Corresponding author. Tel.: +351 22 508 1692.

E-mail addresses: daraujo@fe.up.pt (J.D.P. Araújo), jmiranda@fe.up.pt (J.M. Miranda), apinto@fe.up.pt (A.M.F.R. Pinto), jmc@fe.up.pt (J.B.L.M. Campos).

experimental work on the rising velocity of Taylor air bubbles through a variety of liquids contained in vertical tubes. The authors proposed a general graphical correlation involving Fr , Eo and M numbers, and showed the different regions where the effect of some of the governing forces can be neglected.

Campos and Guedes de Carvalho (1988a) performed a photographic study of the wakes of Taylor bubbles rising through stagnant liquids covering a wide range of viscosities, inside tubes with internal diameter of 19 mm and 52 mm. They reported that the liquid flow pattern in the wake is determined only by the inverse viscosity number (N_f). Three different patterns were identified: for values of N_f below 500, it was observed laminar and closed axisymmetric wakes travelling upwards attached to the bubble tail; when $500 < N_f < 1500$, a transitional regime was reached, where the wakes remained closed but without symmetry around the tube axis; for N_f higher than 1500, the wakes opened and clearly revealed a turbulent behaviour with liquid shedding. The same authors also presented an experimental work regarding the mixing induced by the wakes of air slugs, and compared the results with two different models (Campos and Guedes de Carvalho, 1988b).

A non-intrusive technique combining particle image velocimetry (PIV) and pulsed shadow techniques (PST) was described in detail by Nogueira et al. (2003). This PIV/PST technique was applied to the hydrodynamic characterisation of the flow in the nose region and in the annular film around Taylor bubbles, rising through stagnant and co-currently flowing Newtonian liquids (viscosities in the range of 1×10^{-3} and 1.5 Pa s), inside a vertical tube with 32 mm internal diameter (Nogueira et al., 2006a). Averaged velocity profiles in the liquid ahead the bubble nose and in the film, bubble shapes, and shear stress profiles in the liquid film were reported in detail.

Concerning the flow in the wake of Taylor bubbles, the same authors presented a similar study (Nogueira et al., 2006b). The wake flow patterns (laminar, transitional and turbulent) reported by Campos and Guedes de Carvalho (1988a) were observed, and quantified by means of instantaneous and average flow fields. Values of the wake length and volume were also presented.

Several other experimental works dedicated to the flow of individual Taylor bubbles through stagnant liquids are worth to mention (Polonsky et al., 1999; van Hout et al., 2002; Clanet et al., 2004; Liberzon et al., 2006; Shemer et al., 2007), and allowed the gathering of a substantial amount of information, very useful to understand the hydrodynamics of slug flow. However, the complex features of this flow pattern reveal the limitations on depending solely in an experimental approach, and computation is a crucial tool to solve these limitations and complement experimental studies, enabling a more systematic insight to the physical foundations and providing results with higher precision.

Kawaji et al. (1997) applied the RIPPLE solution algorithm containing the Volume of Fluid (VOF) interface tracking method to simulate the rising of a Taylor bubble through stagnant liquid in a vertical tube, for a unique set of fluid properties. This numerical code was based on the finite difference approximation to solve the governing equations. The flow field was determined only for the liquid phase since the momentum contribution of the gas phase was neglected. A completely different approach was presented by Clarke and Issa (1997), based on an iterative scheme to solve, simultaneously, the velocity and shape of a Taylor bubble, in vertical tubes, along with the flow field. A fitted mesh was generated in each iterative step, with one of its boundaries matching the gas–liquid interface, which excluded the gas phase from the flow field calculations. The main assumptions applied were uniform bubble pressure, and smoothness of the bubble nose. Bugg et al. (1998) presented more detailed results about the motion of Taylor bubbles in vertical tubes. Simulations were performed for different

flow conditions, with a two-dimensional numerical model, incorporating finite difference discretization and the VOF methodology. Bubble shape and rising velocity, liquid film thickness, and complete velocity field in the liquid phase are the main data taken from this work, which were compared with some experimental results. A similar numerical study was conducted by Taha and Cui (2006), taken advantage of the capabilities of the commercial CFD package FLUENT, based on the discretization of the governing equations by the finite volume method, with the VOF methodology already implemented. The authors studied laminar and turbulent flows (RNG $k-\epsilon$ turbulence model) and performed two and three-dimensional simulations, including simulations of tilted columns. The bubble shapes and the Froude number were determined as a function of the Eötvös and Morton numbers.

Lu and Prosperetti (2009) simulated axisymmetric Taylor bubbles rising through stagnant, co-current and counter-current flowing liquids, contained in a vertical tube. The computational code neglected the flow in the gas, and used a finite volume discretization to solve the Navier–Stokes equations, coupled with an interface tracking method based on a set of marker points linked by cubic splines. Very recently, Kang et al. (2010) also applied a front tracking methodology to simulate the dynamics of gas slugs rising through stagnant liquids. The flow in the gas was included in the calculations, and the equations were discretized applying a finite difference method.

Despite the numerical data published, with the exception of the velocity of the Taylor bubble, there is not yet, in the literature, a complete study reporting the influence of the dimensionless Morton and Eötvös numbers in the several hydrodynamic features involved on the flow of individual bubbles rising through stagnant

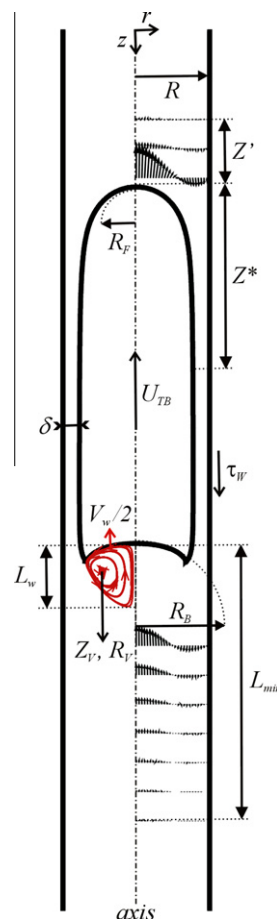


Fig. 1. Illustration of the main hydrodynamic features addressed in the present numerical study.

Newtonian liquids. The main objective of the present work was to perform such a study, with particular emphasis to the liquid wake structure. The computational tool Ansys FLUENT (Release 12.0.1) was exploited to predict, in a detailed way, the variation of the most important slug flow features with M and Eo , in a wide range of conditions within the laminar flow regime. In Fig. 1 is given a global view of the hydrodynamic features focused within this numerical study. These features are the bubble velocity (U_{TB}); frontal bubble radius (R_f); minimum interaction distances above (Z') and below (L_{min}) the bubble; the liquid film thickness (δ) and length needed to have a stabilized film (Z^*); the wall shear stress in the stabilized liquid film (τ_w); the curvature radius of the bubble bottom (R_b); wake volume (V_w) and length (L_w), and the corresponding coordinates of the recirculation core (Z_v, R_v). The accuracy and validity of the numerical code is checked along the work, by performing some comparisons of the simulation results with in-house experimental data (Campos and Guedes de Carvalho, 1988a; Nogueira et al., 2006a,b) and with correlations or theoretical equations available in the literature.

2. CFD model

The commercial CFD package Ansys FLUENT (Release 12.0.1) was used to simulate the flow of a single Taylor bubble through a stagnant Newtonian liquid in a vertical tube. The volume of fluid (VOF) method (Hirt and Nichols, 1981), already implemented in the referred package, was the interface capturing technique employed, along with the geometric reconstruction scheme (Youngs, 1982), which assumes a piecewise-linear approach to represent the interface between phases. The surface tension model used in Ansys FLUENT is the continuum surface force model (Brackbill et al., 1992). The resulting set of governing equations is presented in the software literature.

The simulations were performed in a 2D coordinate system, assuming axial symmetry around the centreline of the vertical tube, in order to minimise computational time and effort. This assumption was made because, in this work, the flow conditions were within the laminar regime. In all simulations, the length of the domain was eleven times larger than the tube diameter. The meshes used to achieve the numerical results were distributed in a uniform way, and consisted on 52×1144 or 104×2288 quadrilateral control volumes. The aspect ratio of the mesh volume elements was approximately one, since it is advisable to obtain a good level of accuracy and grid independence of the geometric reconstruction of the gas–liquid interface.

The simulations were initialized with a bubble shape consisting on a quarter of a circle, corresponding to the bubble nose, connected to a rectangular body with a width equal to the circle radius. The length of the rectangle was always set to be around three times larger than the column diameter, to assure the development of a stabilized liquid film and so, eliminate the influence of the bubble length on the hydrodynamic features under study. For each simulated system, the initial guess for the film thickness, δ , that defines the width of the rectangular body, was obtained from the following equation (Brown, 1965):

$$\delta = \left[\frac{3\nu}{2g(R-\delta)} U_{TB}(R-\delta)^2 \right]^{1/3} \quad (2)$$

where the first guess of the Taylor bubble velocities (U_{TB}) were taken from the corresponding experimental data (White and Beardmore, 1962; Nogueira et al., 2006a) or from a general correlation proposed by Wallis (1969):

$$Fr = \frac{U_{TB}}{\sqrt{gD}} = 0.345 \left(1 - e^{\frac{-0.01N_f}{0.345}} \right) \left(1 - e^{\frac{3.37-Eo}{m}} \right) \quad (3)$$

where $m = 25$ for $N_f < 18$; $m = 69 \cdot N_f^{-0.35}$ for $18 < N_f < 250$; $m = 10$ for $N_f > 250$. These initial estimates for the bubble shape and velocity only affect the convergence time of the simulation to its pseudo-steady state solution. This fact was confirmed by assuming different initial bubble shapes and obtaining the same final numerical results.

Throughout this work, the simulations were performed in a frame of reference attached to the rising Taylor bubble (moving frame of reference - MFR). With this frame of reference, the tube wall moves downward at a velocity (U_{wall}) equal to the bubble rise velocity (U_{TB}). Additionally, it was imposed the no-slip condition on the tube wall. At the top of the domain, an inlet flow boundary was used, with liquid entering at an average velocity equal to the velocity of the bubble motion in a fixed frame of reference ($U_{in} = U_{TB}$). In this inlet boundary, the velocity profile is assumed as uniform, since the simulations were performed for stagnant liquids. On the axis of the tube, symmetry boundary conditions were applied (zero normal gradients for all variables). At the bottom of the computational domain, an outflow boundary condition was assumed, since there is only liquid exiting, and the domain is large enough to ensure that a uniform velocity profile is restored.

When the wall and inlet boundary conditions are defined with a correct value of U_{TB} , the Taylor bubble should become stationary. For each flow condition studied, the experimental or estimated value of U_{TB} was used as an initial guess, which was then adjusted until the nose of the bubble stopped moving in the axial direction. In Fig. 2, the boundary and initial conditions described in this section are schematically compiled.

Within this CFD package, it was applied the pressure-based solver, where a finite volume methodology is used to discretize the equations. The PISO (pressure-implicit with splitting of operators) was the chosen pressure–velocity coupling scheme, and the pressure interpolation method applied was the pressure staggering option (PRESTO!). The QUICK scheme was used for solving the momentum equation. The gradients of scalars were computed according to the Green-Gauss node-based method, which is known to be more accurate than the cell-based method.

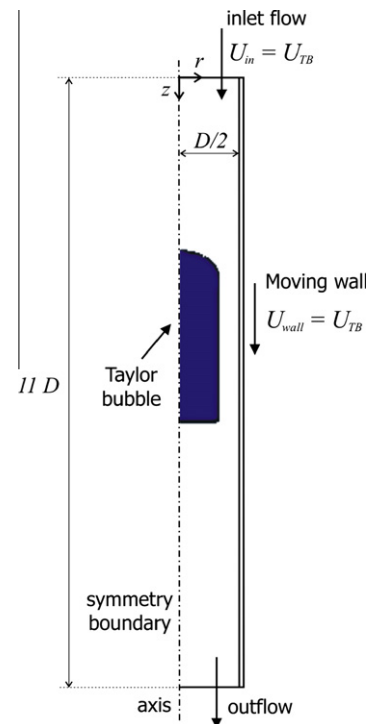


Fig. 2. Schematic representation of the domain, boundary and initial conditions.

The equation for the volume fraction was solved with an explicit time-marching scheme, for a maximum Courant number set to 0.25, and was spatially discretized by the geometric reconstruction approach. This approach is recommended for VOF simulations, due to its higher accuracy and ability to render clear and well defined interfaces, without numerical diffusion. When simulating multiphase flows with large body forces, like gravity acting on phases with high density differences, segregated algorithms can have convergence problems if special care is not taken. To tackle this issue and guarantee more robust solutions, the optional implicit body force treatment was used. A variable time step was applied to the governing equations, based on a global Courant number fixed to 0.25, with a maximum number of iterations of 1000. The scaled absolute values of the residuals, for velocities and continuity, were monitored and set to 10^{-6} as a convergence criterion for each time step.

3. Results and discussion

An extensive numerical study was performed to describe the flow of a single Taylor bubble rising through vertical columns of stagnant liquids. For that purpose, several simulations were made for a set of different Morton numbers, based in the work of [White and Beardmore \(1962\)](#), and covering a wide range of Eo . The computed results were analysed in detail, and the main information is presented throughout this section, divided into four main parts: Taylor bubble velocity; flow around the bubble nose; liquid film; and wake region.

Before advancing into the referred analysis, it is important to provide a global perspective about the influence of the relative magnitude of the acting forces (inertia, buoyancy, surface tension and viscous) on the bubble shape and on the surrounding flow field. To better visualise these effects, the obtained bubble shapes, numerical velocity fields and streamlines (for both liquid and gas phases), for a wide spectrum of flow conditions are compiled in [Fig. 3](#) and presented in the form of a matrix. The type of graphical representation used to describe each flow field was inspired in the work of [Kang et al. \(2010\)](#), and is defined for a moving frame of reference (MFR) attached to the bubble. The dimension of the vectors presented are not proportional to their real magnitude, when comparing the flow fields between different cases, since the purpose of [Fig. 3](#) is to give only a qualitative image of their variation with M and Eo . Instead, for each case, a constant value of the ratio between the vector lengths and their magnitude is adjusted, taken the correspondent maximum magnitude as reference. This allowed a clearer representation about the details of the flow fields, in the systems shown throughout the entire matrix. Each row of this matrix corresponds to a constant Morton number, where the different columns are represented by an Eötvös number that varies from around 6 to 575.

Prior to any discussion about the matrix presented in [Fig. 3](#), it is important to refer that, for each Morton number, the chosen range of Eo was limited to the set of simulations that revealed an absence of small bubble liberation. In fact, for the simulations with Eo higher than the ones presented in [Fig. 3](#), it was verified a release of small amounts of gas from the tip of the bubble tail. In some tested cases, this liberation was eliminated by the use of an extra-refinement in the mesh, which suggests an issue of numerical nature that needs to be further investigated in future work.

Looking at the bubble shapes, there are three general observations that must be pointed out:

- As it was expected, the nose and tail of all bubbles consist on prolate and oblate spheroids, respectively, where the curvature of the tail seems to exhibit a higher sensitivity than the nose to the influence of viscous and surface tension forces.

- For a constant Morton number, as the predominance of surface tension forces decreases (Eo increases) the convex shape of the tail flattens, and eventually changes to a concave shape relative to the liquid phase.
- Fixing the value of Eo , when the importance of the viscous forces diminishes (M decreases), the concavity of the tail presents a similar behaviour to the one described in the previous point. This is easy to verify in [Fig. 3](#), since as the Morton number decreases, the flattening of the tail and inversion to a concave shape occurs at lower values of Eo .

Regarding the flow field inside the bubbles, it simply consists on a large recirculation zone. With much larger relevance for the purpose of this work is the flow field in the liquid phase that surrounds the Taylor bubble. From the graphical representations shown in [Fig. 3](#), the main observation concerning this aspect is the presence of a wake region in some cases. The appearance and size development of this region follows the same evolution trends previously referred for the concavity of the bubble tail.

A preliminary validation of the numerical code was intended by reproducing one of the experiments reported in [Nogueira et al. \(2006a, 2006b\)](#), for a system with stagnant liquid, M of 4.31×10^{-2} and N_f of 111 (within the laminar regime). In [Fig. 4](#), the resulting numerical velocity fields and streamlines are presented, together with a direct comparison, performed in the three main flow regions (above the bubble nose, liquid film and wake region), between numerical and experimental dimensionless axial velocity profiles (u_z/U_{TB}) in a fixed frame of reference (FFR).

Concerning the zone above the bubble nose and the wake region, numerical and experimental data of u_z/U_{TB} profiles were taken for two different axial iso-surfaces, where the z/D coordinate is referenced to a point placed in the bubble nose and in the tip of the tail, respectively. The simulation data seem to match relatively well the behaviour of the experimental velocity profiles, particularly in the region above the nose. In the wake region, the simulation overpredicts a little bit the experimental profiles, probably due to the difficulty of the experimental techniques on defining the position of the bubble tip with precision.

As depicted in the middle right side of [Fig. 4](#), the dimensionless numerical profiles are in a fair agreement with the experimental u_z/U_{TB} . The visible errors closer to the bubble interface (smaller r/D) reflects the deviations that exists between the simulation and experimental data of U_{TB} and δ – 8.5% and 2.8%, respectively. To clarify this fact, the u_z/U_{TB} profile predicted by Brown's theory ([Brown, 1965](#)) was also plotted, and it reveals to be much closer to the corresponding numerical data. This theory consists on combining Eq. (2) with the following expression:

$$u_z = \frac{g}{v} \left[\frac{R^2 - r^2}{4} - \frac{(R - \delta)^2}{2} \ln \frac{R}{r} \right] \quad (4)$$

3.1. Taylor bubble velocity

A separate part of this work is here dedicated to the analysis of the results for the bubble rising velocity, due to the enormous relevance of this hydrodynamic feature in the description of vertical slug flow systems.

Experiments were conducted by [White and Beardmore \(1962\)](#) in several gas–liquid systems, corresponding to a vast range of Morton numbers. Some of these values of M were taken as reference to this work and, by varying the tube diameter, a large number of simulations was performed to cover a spectrum of Eo as wide as possible. For the totality of the simulated systems, in the definition of the fluid properties and tube diameter, it was also taken into account that the laminar regime should prevail. According to [Campos and](#)

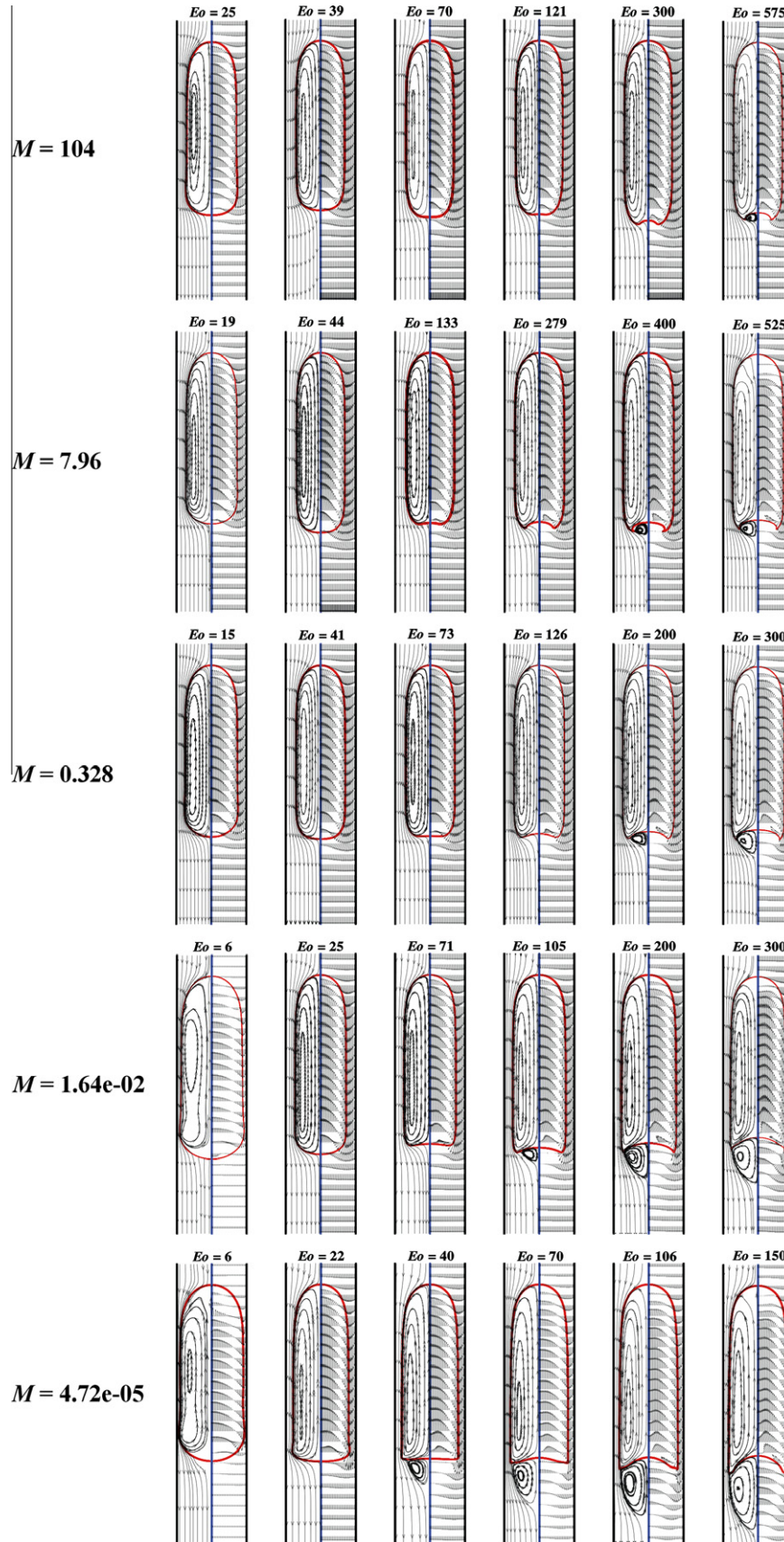


Fig. 3. Compilation of numerical velocity fields, streamlines and bubble shapes for a wide range of flow conditions. Representation inspired in Kang et al. (2010).

Guedes de Carvalho (1988a), to assure a wake region with laminar flow, the inverse viscosity number (N_f) ought to be less than 500.

Concerning the liquid film region, literature is not clear about the definition of an exact value for the critical Reynolds number

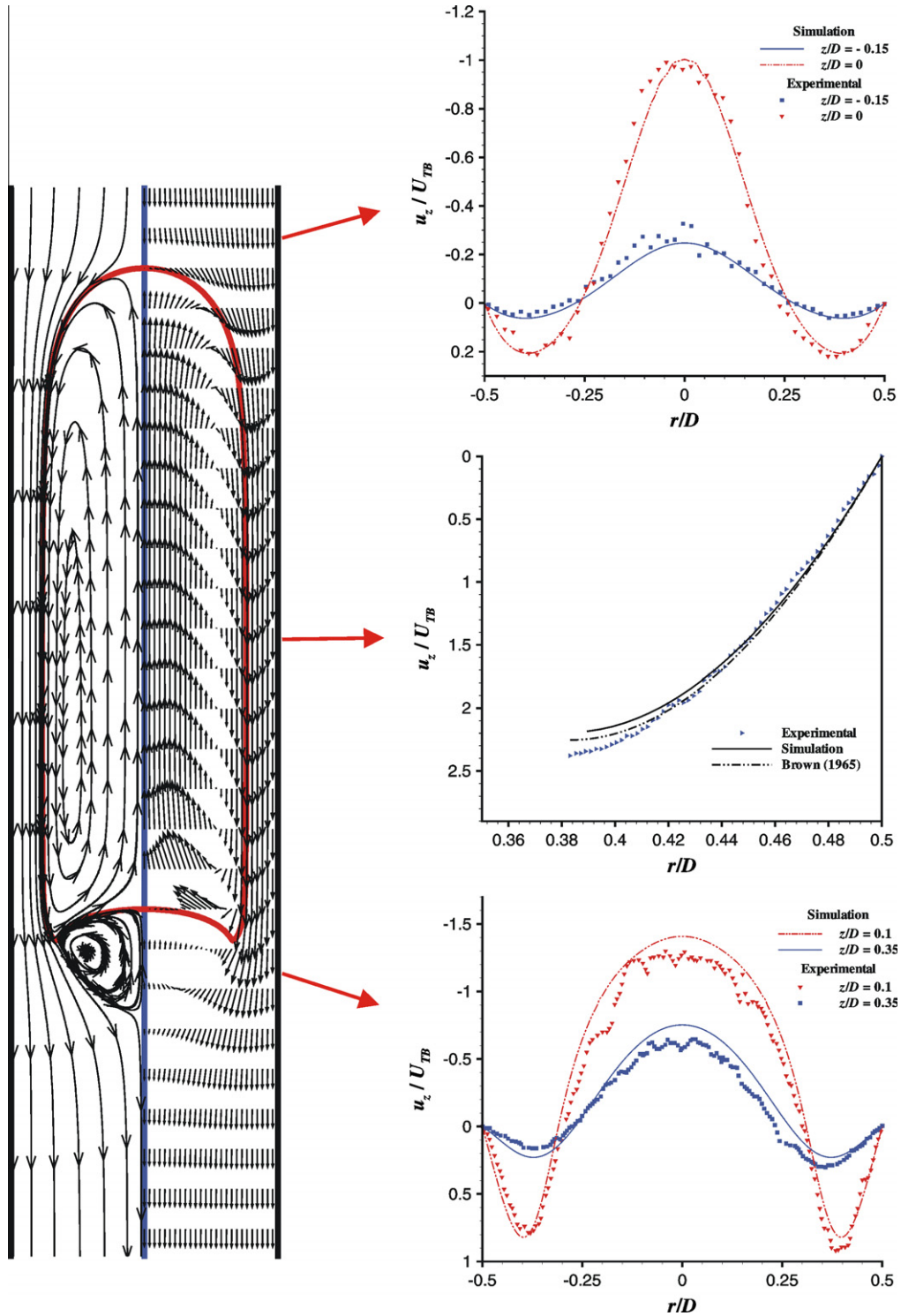


Fig. 4. Numerical velocity fields and streamlines for a system with M of 4.31×10^{-2} and N_T of 111. Numerical and experimental dimensionless axial velocity profiles (u_z/U_{TB}), in a fixed frame of reference (FFR), are also plotted for different axial iso-surfaces in the three main flow regions: above the bubble nose (upper right), developed liquid film (middle right) and wake region (lower right).

($Re_{U_\delta} = \rho \cdot U_\delta \cdot \delta / \mu$, where U_δ is the average liquid velocity in the liquid film), where laminar–turbulent transition occurs, since the published data is somewhat scattered between 250 and 800 (Fulford, 1964). Nevertheless, in the entire set of flow conditions under study, the Re_{U_δ} never exceeds 60, which guarantees that the developed liquid films are fully laminar.

Regarding the Taylor bubble velocity, the numerical data obtained in this set of simulations is depicted in Fig. 5, in the form

of Froude number as a function of Eo and M . For the same Morton numbers, the curves predicted by two different correlations are also shown: the first one proposed by Wallis (1969) – Eq. (3); and the second one taken from a broader and more recent work reported by Viana et al. (2003) – Eq. (5). Experimental data collected from White and Beardmore (1962), regarding some flow conditions numerically reproduced in this work, was also added to Fig. 5 for comparison purposes.

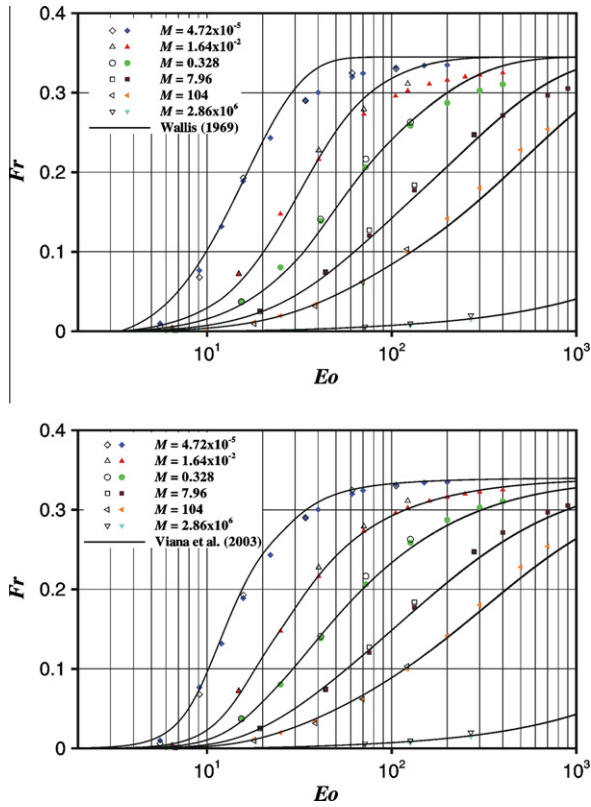


Fig. 5. Numerical results (closed symbols) of U_{TB} for a set of different Morton numbers and several Eo . The curves predicted by the correlations of Wallis (1969) and Viana et al. (2003) are shown in the top and bottom graphics, respectively. Experimental data (open symbols) from White and Beardmore (1962) was also added to both graphs.

$$Fr = \frac{0.34 / (1 + 3805 / Eo^{3.06})^{0.58}}{\left(1 + \left(\frac{R_G}{31.08} \left(1 + \frac{778.76}{Eo^{1.96}}\right)^{-0.49}\right)^{-1.45} \left(1 + \frac{7.22 \times 10^{13}}{Eo^{9.93}}\right)^{0.094}\right)^{0.71} \left(1 + \frac{7.22 \times 10^{13}}{Eo^{9.93}}\right)^{-0.094}} \quad (5)$$

$$\text{where } R_G = \sqrt{D^3 g (\rho_L - \rho_G) \rho_L / \mu_L}.$$

From the observation of Fig. 5, the first aspect worth noting is a clear separation of the data between the different Morton numbers considered. This aspect is due to a growing relevance of the viscous forces on the Taylor bubble velocity, as the value of M increases. For values of M even lower than 4.72×10^{-5} , the curves would merge into a single line, which is typical for very dilute aqueous solutions. However, these conditions are outside the scope of this work, since it would lead to turbulent regimes. It is also visible in Fig. 5 that the CFD code produced results of U_{TB} that fits reasonably well the behaviour expected by the correlations, applied for each value M , starting from a region where surface tension dominates and the bubble tends to stop ($Eo < 3.37$), up to a region where the inertial forces are predominant (high Eo).

Furthermore, the correlation of Viana et al. (2003) is the one predicting velocities much closer to the presented numerical results. As it can be seen in Fig. 6, if a parity plot of the U_{TB} simulation data and the bubble velocity predicted by Eq. (5) is sketched, the agreement is unquestionable. The large spectrum of performed simulations provided numerical results of U_{TB} that are within a 10% deviation from the predictions calculated with the correlation of Viana et al. (2003). However, two exceptions must be pointed

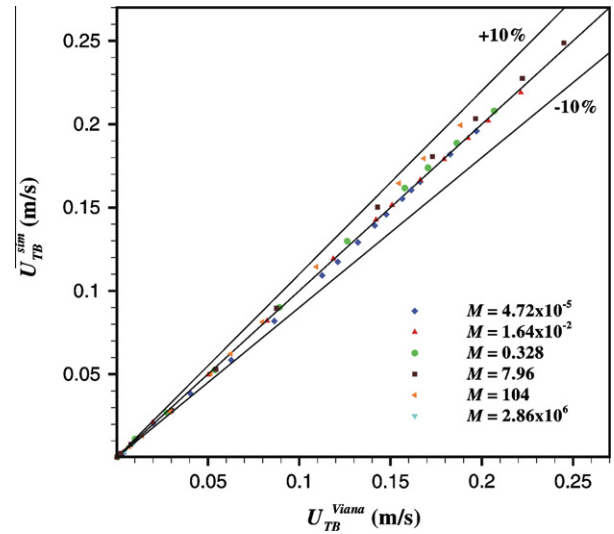


Fig. 6. Parity plot of the Taylor bubble velocities obtained by the correlation of Viana et al. (2003) and the numerical code.

out, since they are not easy to detect in Fig. 6, due to scaling effects. The first exception concerns the simulations made for Eo around 6, where the deviations were between 16% and 35%. Two factors may contribute to this kind of deviations: very low values of U_{TB} (bubble is almost stopped) that are much more sensitive to small numerical errors; and since the lower limit of application of Eq. (5) is also for an Eötvös number of 6, the correlation can introduce another source of uncertainty for these cases. The second exception regards the systems with very high viscous forces ($M = 2.86 \times 10^6$), where the deviations were in the range of 6–19%. In these situations, the problem is most probably numerical, since it is predictable that the code starts to experiment some difficulties for very high viscosity ratios between the two phases under simulation. Considering this reason, the cases for a Morton number of 2.86×10^6 were excluded from the detailed analysis to be performed in the following sub-sections.

The simulation results of U_{TB} also compares favourably with the experimental data (White and Beardmore, 1962) presented in Fig. 5. In fact, excluding the exceptions referred above (very low Eo , and M of 2.86×10^6), the deviations between numerical and experimental Taylor bubble velocities are within the 10% range.

3.2. Flow around the bubble nose

Beginning with the shape of the gas–liquid interface itself, in the set of simulations performed for Morton numbers between 4.72×10^{-5} and 104, the shapes obtained for the bubble nose were characterised by the estimation of the mean curvature radius, also known as frontal radius (R_F). The purpose was to infer if this feature suffers any influence from a variation in the relative magnitude of the acting forces. Although the entire nose of a Taylor bubble is normally described by an ellipsoid, and its rising velocity was successfully modelled by assuming an ovary ellipsoidal shape (Funada et al., 2005), the approach here applied to determine the frontal radius was simplified to the circumference geometry. It was admitted that in a small region of the bubble front end – with axial coordinates confined between the tip of the nose up to 0.5 maximum bubble radius (R_{TB}) below – its shape could be defined by a small arc of a circle, whose radius was considered to be a fair estimate of the frontal radius. The maximum bubble radius is obtained by subtracting the stabilized liquid film thickness (δ) to the column radius:

$$R_{TB} = R - \delta \quad (6)$$

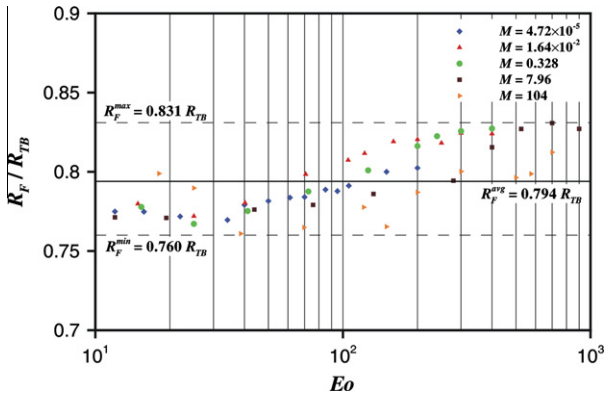


Fig. 7. Dimensionless numerical frontal radius (R_F/R_{TB}) for a set of different Morton numbers over a wide range of Eo (solid points). Horizontal lines are placed to indicate the maximum and minimum R_F values obtained (dashed lines), and their arithmetic average (solid line).

The numerical results of the frontal radius, based on the simplification just described, are graphically presented in Fig. 7.

Looking at Fig. 7, although the R_F/R_{TB} results seems to have a shy tendency to increase with Eötvös number (particularly for Eo above 40), the difference between the minimum and maximum values is very narrow (around 8%). By these reasons, it is assumed a mean frontal radius of $0.794R_{TB}$ as the final result. This result is not far from the conclusions reported by Brown (1965), that suggests, for several liquids, the value of $0.75R_{TB}$. The small spread of the presented frontal radius data around a mid value can be explained by two aspects: the numerical gas–liquid interface is admitted to be where the gas volume fraction is 0.5, leading to a node interpolation on determining its correct position, which is more sensitive to deviations in regions where the curvature is more pronounced; the adjustment of the circumference equation to the numerical position of the gas–liquid interface (from the tip of the bubble nose up to a downward distance of $0.5R_{TB}$), using R_F as the fitting parameter, is a simplification, already assumed, that can introduce a small level of inaccuracy. However, the possible fitting inaccuracies, just pointed out, are within very reasonable limits, as it can be proved by the visualisation of Fig. 8.

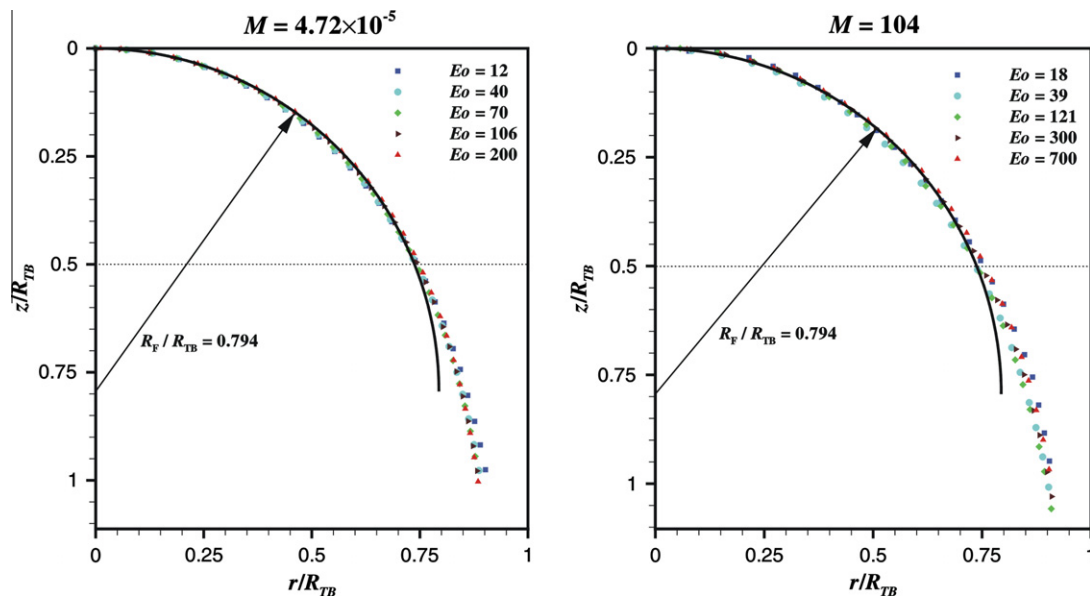


Fig. 8. Simulation results of the nose bubble shape (filled points), for sets of different Eo , within the lower and higher Morton numbers under analysis (4.72×10^{-5} and 104). The circle corresponding to the average frontal radius of $0.794R_{TB}$ is presented (solid line), and the dotted line indicates the upper limit of z/R_{TB} used for the fittings.

In Fig. 8, shapes of the Taylor bubble numerical front end are represented for the higher and lower values of M under the scope. For each one, a set of five different Eo was chosen, and the shapes obtained by simulation are defined by filled points (with an index skip of 4 in the axial direction). Dimensionless coordinates were applied using the corresponding value of R_{TB} , and the origin of the axial position was placed in the tip of the bubble nose. The main observation taken from Fig. 8 is that, inside the fitting limits of z/R_{TB} , the circumference defined by the average frontal radius ($0.794R_{TB}$) compares very favourably with all the numerical bubble front ends presented. Besides that, it is also a fact that up to an axial distance of $0.5R_{TB}$, starting from the nose tip, and using dimensionless coordinates, the referred bubble front ends are almost overlapped, which reveals a high degree of independence from the flow conditions, much like it was already claimed by Brown (1965).

Finally, to close the analysis regarding the flow around the Taylor bubble nose, the numerical results of the length ahead of it necessary to stabilize the liquid flow field (Z') are presented in Fig. 9. The results of Z'/D were plotted as a function of the inverse viscosity number (N_f), since this representation reveals itself more clearer and, within the simulated range, is almost independent of the Morton number (with the exception of M equal to 4.72×10^{-5}). The criterion used to estimate the values of Z'/D was based on determining the region where the normalised difference between u_z on the column centreline and the rising velocity, in a fixed frame of reference (FFR), has an absolute value greater than 0.01 ($|u_z - U_{TB}|/U_{TB} > 0.01$).

Looking at Fig. 9, it is easy to notice that the results can be roughly divided into two main regions:

- For lower values of the inverse viscosity number (below 40), the results of Z'/D are almost independent of M and N_f , and approximately equal to 0.483;
- For higher inverse viscosity numbers, the values of Z'/D seems to increase linearly with the natural logarithm of N_f . Within a range of M between 1.64×10^{-2} and 104, the results of Z'/D can be reasonably well described by a single equation – equation (B) in Fig. 9. In fact, the data obtained suggests almost a unique functionality between Z'/D and N_f , suffering only a slight influence of the Morton number. With a close observation, this

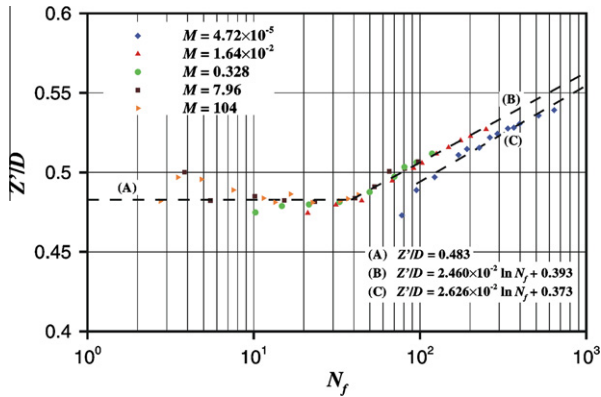


Fig. 9. Simulation results of Z/D (filled points) as a function of N_f in logarithmic scale, for a set of five Morton numbers. The dashed lines represent fittings of the numerical data of Z/D , for different ranges of N_f and M .

influence was noticed to increase gradually as M decreases, being perceptible only for the lower Morton number under study (4.72×10^{-5}), which led to a separate fit of the corresponding Z/D data – equation (C) in Fig. 9. It means that Z/D depends not only on the ratio between gravitational and viscous forces, but also on the inertial and surface tension forces. To understand the trend of Z/D , one must take into account variations in the bubble radial dimension, since a larger diameter can force the deflection of the streamlines at higher distances from the tip of the bubble. As it can be later observed, when addressing to the dimensionless stabilized film thickness (δ/D), for higher N_f numbers (above the range of N_f between 10 and 100), the bubble diameter increases (the thickness of the film decreases), and that, for lower Morton numbers, this increase takes place for later inverse viscosity numbers. This film thinning, result of the balance of the different forces, seems to be related with the increase of Z/D .

3.3. Liquid film

The flow in the liquid film will be characterised by aspects related to three main features: the film developing length (Z^*), the stabilized liquid film thickness (δ) and the wall shear stress (τ_w).

Starting with the length needed to stabilize the flow below the bubble nose, the numerical results were converted into a dimensionless form (Z^*/D) and are presented in Fig. 10. These results were obtained at the radial midpoint of the fully developed film, and by the application of a criterion based on two quantitative necessary conditions:

- The derivative of u_z with respect to z/D , in the fully developed region, should be less than 5% of the maximum slope achieved along the developing film – this implies that, for distances higher than Z^* , the slope of the u_z curve is almost zero, which means that the axial velocity is stabilized within an acceptable margin of error.
- The radial component of the velocity, normalised by the maximum u_r obtained along the film, must be smaller than 5% – this condition is set to assure that the values of the radial velocity are almost negligible in the developed film.

Much like what happened with the flow stabilization length ahead of the bubble nose, the results of Z^*/D were also divided into two regions. Although this similar behaviour, there is a significant difference that must be pointed out: the values of Z^*/D seems to be independent of the Morton number, on the entire range of the simulated conditions. This means that Z^*/D depends solely on the

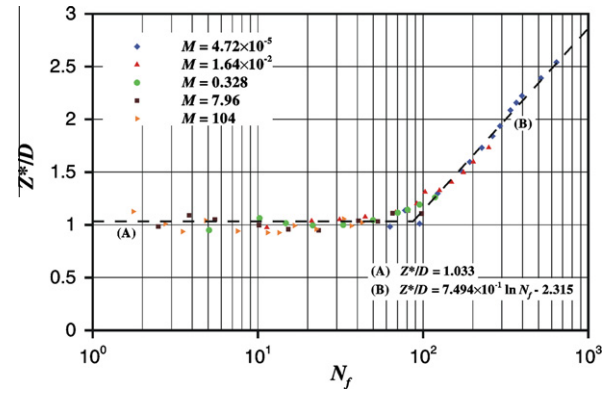


Fig. 10. Numerical results of Z^*/D (filled points) as a function of N_f in logarithmic scale, for a set of five Morton numbers. The dashed lines represent fittings of the numerical values of Z^*/D , for different regions of N_f .

inverse viscosity number, with particular emphasis for N_f higher than 80–90. Mathematically, it can be expressed by the following equations:

$$\begin{aligned} Z^*/D &= 1.033 \quad \text{for } N_f < 90 \\ Z^*/D &= 7.494 \times 10^{-1} \ln N_f - 2.315 \quad \text{for } N_f > 90 \end{aligned} \quad (7)$$

Stepping into the fully developed film, the most important hydrodynamic feature to analyse is the stabilized liquid film thickness (δ). In Fig. 11, the numerical results of the dimensionless film thickness (δ/D) are compiled for different Morton numbers as a function of N_f . Regarding the Morton numbers under the scope, the curves of δ/D versus N_f were estimated and placed in Fig. 11, just to have an idea of the behaviour that should be expected for this dimensionless feature. This estimation was performed by combining the correlation of Viana et al. (2003), to obtain the bubble velocity, with the equation of Brown (1965) for the liquid film thickness – Eq. (2).

Looking at Fig. 11, the first thing to notice is the proximity of the numerical results to the predicted curves of δ/D . For each Morton number, these curves present a maximum and, when increasing N_f , a region that can be translated as a decreasing exponential func-

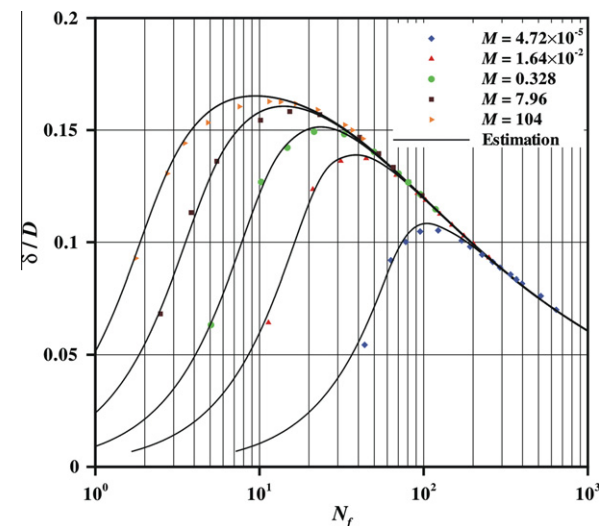


Fig. 11. Variation of the dimensionless liquid film thickness (δ/D) with N_f (logarithmic scale), for a set of five Morton numbers. The solid lines were estimated by the combination of the work of Viana et al. (2003), regarding U_{TB} , with the equation defined by Brown (1965) to predict the developed liquid film thickness.

tion of the inverse viscosity number, which is common to all curves. This region grows and the maximum of δ/D gets higher as the value of M increases.

Another important issue to refer is that Kang et al. (2010) already defined δ/D as a function of Ar ($= N_f^2$), independent of the Morton number. As it can be easily seen in Fig. 11, this conclusion is limited only for some ranges of Ar (or N_f), and the extent of those ranges are also strongly dependent on M .

In order to confirm the reliability of the simulation results related to the developed liquid film, the numerical axial velocity profiles were compared to the corresponding theoretical ones. These theoretical profiles were based on the values of δ estimated by Eq. (2), and in expression (4) deduced by Brown (1965).

The numerical and theoretical u_z profiles were converted to the fixed frame of reference (FFR), normalised with the appropriate bubble rising velocity, and plotted together as a function of the dimensionless radial coordinate (r/D). In Fig. 12, the resulting u_z/U_{TB} profiles are presented for different sets of Eötvös numbers, organised into four values of M .

As depicted in Fig. 12, the numerical u_z/U_{TB} profiles are almost in perfect agreement with the theoretical predictions. The only visible exception is the system with lower Eo ($=18$) for a Morton of 104, where the maximum deviation does not exceed 4%. This observation reinforces the idea that the CFD code applied is very precise on simulating the systems under study.

The wall shear stress is a particularly relevant feature if slug flow occurs simultaneously with heat or mass transfer, governing

these phenomena when involved in processes like membrane separations (Taha and Cui, 2002) or flow induced corrosion in pipe wells (Villarreal et al., 2006; Nešić, 2007). In Fig. 13 is illustrated how the behaviour of the wall shear stress is influenced by the presence of a Taylor bubble. In a similar manner to what was made for the u_z profiles, inside the liquid film, the evolution of the dimensionless wall shear stress – $\tau_w/(\rho_l g D)$ – is represented along the distance from the bubble nose (z/D), for several pairs of Eötvös and Morton numbers.

Generally, the wall shear stress starts to increase near the bubble nose until it reaches a kind of plateau. This is consistent with the formation of a stabilized liquid film, since τ_w should be highly dependent on the variation, along the axial coordinate, of the gap that exists for the liquid phase to flow between the Taylor bubble and the wall. For this reason, when the liquid thickness increases again, as it approaches the bubble tail, a pronounced decrease on the wall shear stress was confirmed by the numerical results. However, it is visible that some exceptions to this general behaviour occurred for the lower values of Eötvös number. For these situations, the wall shear stress presents a peak immediately below the stabilized liquid film. It is explained by an inflection from the standard shape of the gas interface, near the bubble tail, forming a bulge typical for systems with low Eo . As the Morton number decreases, the referred peaks become higher, since the values of the stabilized dimensionless film thickness (δ/D) are getting smaller, which gives to the bulge formation a deeper influence on the variation of τ_w . Another aspect, that was detected only in the situations of higher

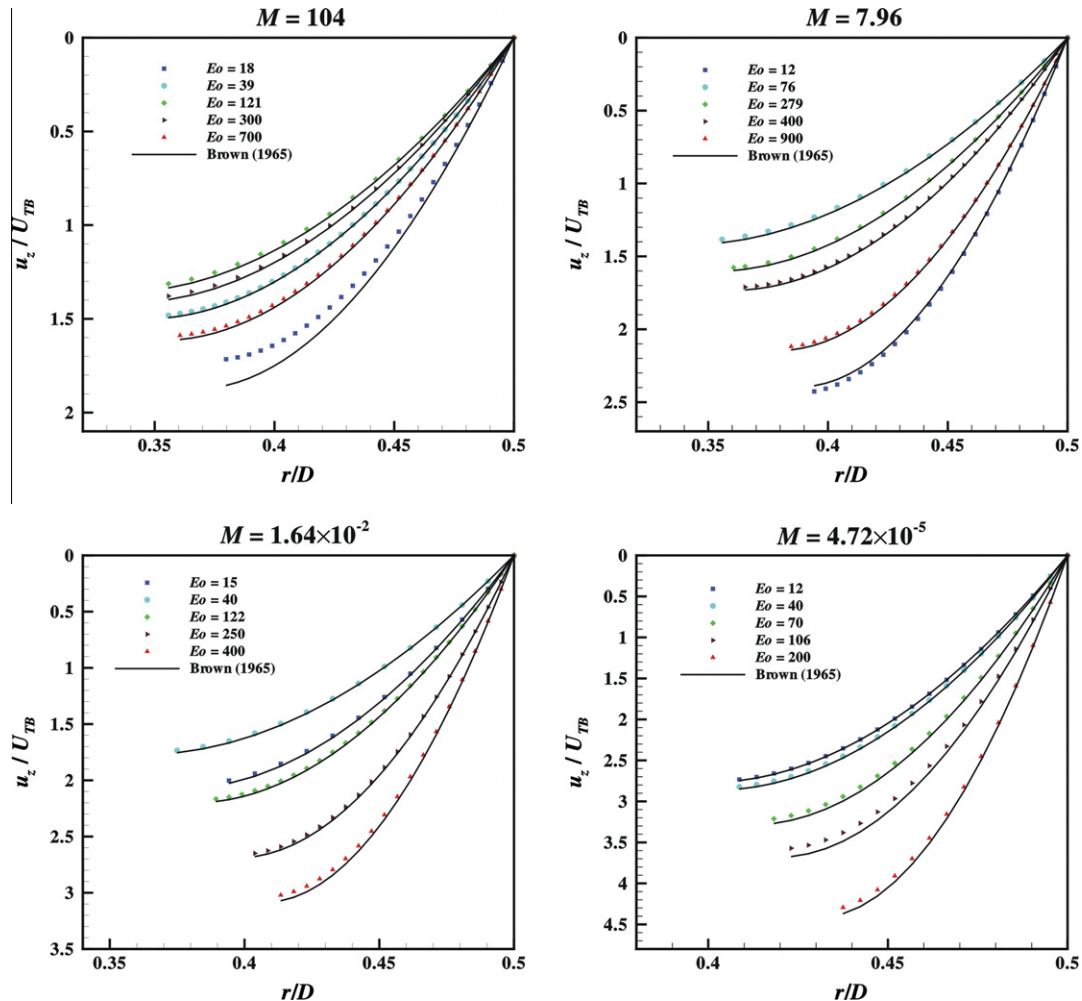


Fig. 12. Dimensionless axial velocity profiles (u_z/U_{TB}) inside the developed liquid film, for sets of different Eo , within four Morton numbers under analysis (4.72×10^{-5} , 1.64×10^{-2} , 7.96 and 104). For each flow condition presented, the axial velocity profile predicted by Brown (1965) is also shown (solid lines).

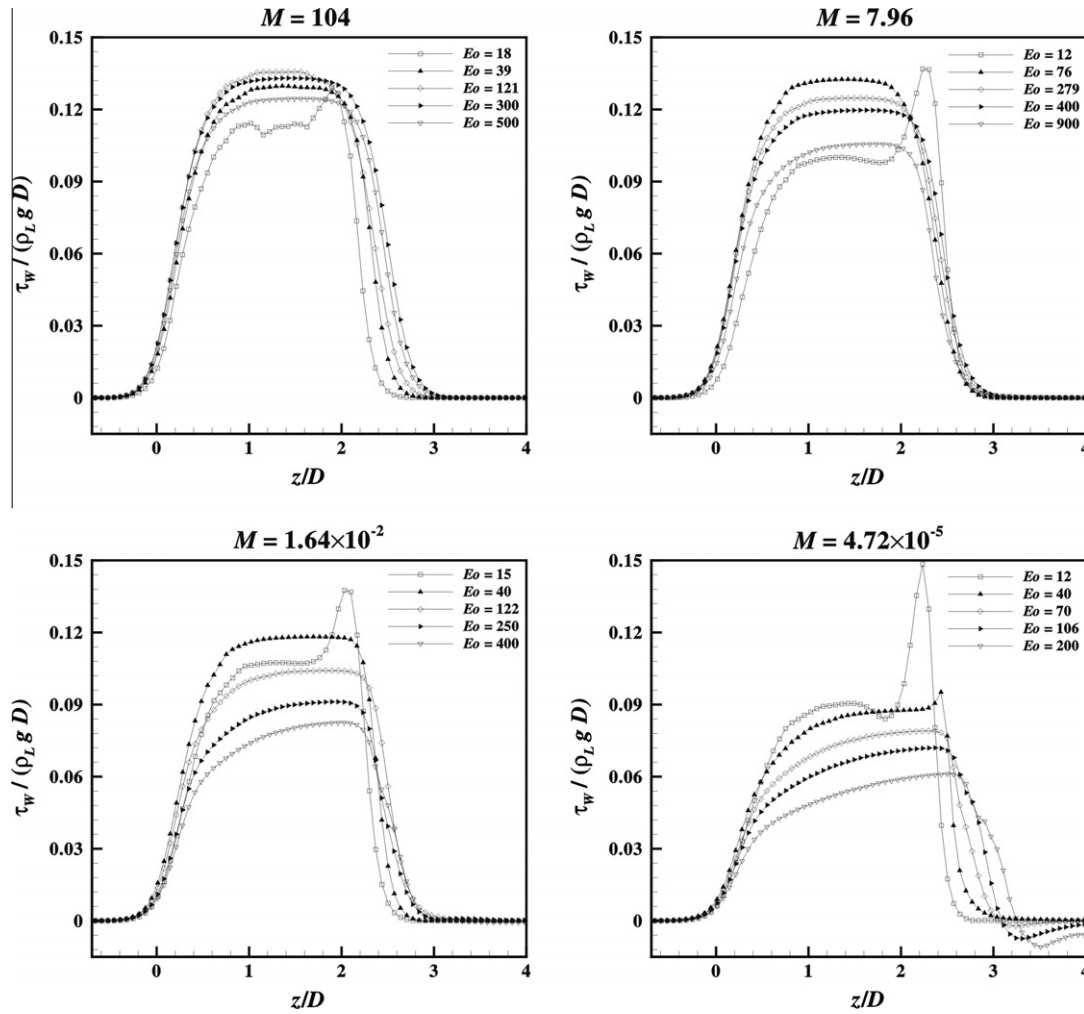


Fig. 13. Dimensionless wall shear stress ($\tau_w/(\rho_L g D)$) along the axial distance from the bubble nose (z/D), for different Eötvös numbers, within four values of M (4.72×10^{-5} , 1.64×10^{-2} , 7.96 and 104).

Eo , within the M of 4.72×10^{-5} , is the presence of negative values of wall shear stress near the wake region. It seems that, for some distance below the bubble bottom, the liquid phase close to the wall is flowing upwards (in a FFR), which produces stresses in the opposite direction of what was obtained in the majority of the simulated systems. This occurrence will be deeply inferred in the section regarding the flow in the wake region.

Focusing on the wall shear stress in the region of the stabilized liquid film, this feature can be predicted using the previously estimated values of δ , and combining the equation for the theoretical axial velocity profiles deduced by Brown – Eq. (4) – with the definition of shear stress applied to the wall:

$$\tau_w = -\mu \left. \frac{du_z}{dr} \right|_{r=R} = \rho_L g \left[\frac{R}{2} - \frac{(R-\delta)^2}{2R} \right] \quad (8)$$

The numerical results of τ_w were converted into the dimensionless form, and their evolution with N_f is presented in Fig. 14, together with the corresponding curves predicted by the procedure just described.

Similarly to what happened with δ/D , the numerical results are very near the predicted curves. The larger deviations are mainly concentrated in the region of the lower values of N_f , corresponding to the lower Eo (for each Morton number). In these systems occurs the formation of a bulge near the bubble tail, already explained, which could also be responsible for the referred deviations, since

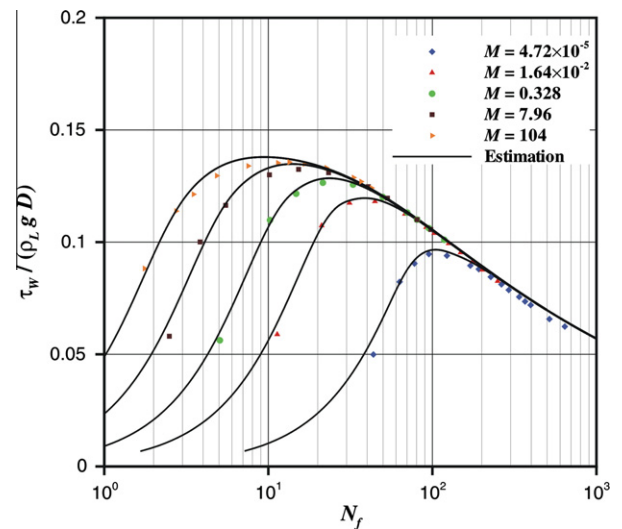


Fig. 14. Dimensionless wall shear stress ($\tau_w/(\rho_L g D)$), inside the developed liquid film, as a function of the inverse viscosity number, in logarithmic scale, for a set of five Morton numbers. The solid lines were estimated by the combination of the work of Viana et al. (2003), regarding U_{TB} , with the theory proposed by Brown (1965).

it implies that the wall shear stress plateau, observed in the liquid film, is less stabilized or even unstable.

Looking with more attention to Figs. 11 and 14, the behaviour of $\tau_w/(\rho_l g D)$ with the inverse viscosity number is very similar to the one noticed for δ/D . A dependency between the dimensionless wall shear stress and the liquid film thickness was predictable since, in order to isolate these parameters, a further manipulation of Eq. (8) leads to:

$$\frac{\tau_w}{\rho_l g D} = \frac{\delta}{D} \left(1 - \frac{\delta}{D}\right) \quad (9)$$

With the functionality expressed in Eq. (9), it is easy to conclude that for low δ/D values, the corresponding dimensionless wall shear stresses should have almost the same value. Regarding the data presented in Figs. 11 and 14, both numerical and predicted values seem to agree with this conclusion in the extremities of the N_f axis, which is where the dimensionless liquid film thickness data is lower. This is another sign to firm the coherence of the simulation results attained.

Likewise what was described for δ/D , Kang et al. (2010) presented the dimensionless wall shear stress as a single variable function of the Archimedes number. The authors reported that $\tau_w/(\rho_l g D)$ depends linearly on the logarithm of Ar , which is consistent with only a part of the data presented in Fig. 14. Again, it is important to notice that the conclusion taken in the referred work (Kang et al., 2010) is applicable only to some regions of Ar , depending highly on the Morton number.

3.4. Wake region

In the majority of the operating conditions, the liquid flowing around the Taylor bubble leaves the annular film and creates a recirculation zone, behind the bubble rear, which is commonly known as wake region. Detailed understanding of the wake flow pattern is decisive, since it can play an important role on the interaction between consecutive Taylor bubbles.

Due to the high relevance on studying the wake structure with feasible data, the first step of this section was to perform a comparison between experimental wake and bubble tail shape with simulations, using results taken from the work of Campos and Guedes de Carvalho (1988a). This comparison was made for five different conditions – (a)–(e) – corresponding to N_f of 176, 205, 325, 437 and 483, respectively. In order to achieve a meaningful comparison, each photo and the corresponding numerical bubble interface were converted to the same metric scale, before performing the superimpositions presented in Fig. 15. The scale references for these conversions were the reported experimental bubble lengths (Campos and Guedes de Carvalho, 1988a), measured along the tube axis, and the mesh boundary limit in the radial axis, which is the column radius (9.5 mm).

Based on the visualisation of Fig. 15, it is fair to claim that the numerical bubble rear ends are a reasonable fit to the experimental ones. Adding to the tail shape data, the amount of tracer visible in the photos of the experimental bubbles also enables a preliminary check regarding the quality of the numerical wake dimensions. In quantitative terms, the absolute deviations between experimental and numerical results of L_w and V_w are within the intervals of 1–14% and 4–11%, respectively. Considering that the experimental technique consists on dye transportation inside the wake, whose accuracy can be clearly limited by diffusion, it is fair to say that the magnitude of the deviations is quite acceptable. These arguments are a proof of the ability of the numerical code to correctly reproduce wake experimental data for different operating conditions.

Returning to the set of simulations serving as base to this work, and in analogy with Section 3.2, the gas–liquid interface of the bubble tail is analysed first. For that purpose, the shape of the

bubble bottom and the corresponding curvature radius (R_B), obtained in the simulations with the lower Morton number (4.72×10^{-5}), are represented in the following graphs (Fig. 16). The numerical results regarding this value of M were chosen to better illustrate the role of Eötvös number, since it was observed an increased sensitivity of the bubble tail to Eu when decreasing the Morton number.

With the illustration placed on the left side of Fig. 16, it becomes clear the importance of Eu to the shape of the bubble bottom, particularly referring to systems with values of M in the range of 10^{-5} or below. The numerical shapes presented were defined by extracting the simulation results of the interface coordinates around the tail region, putted in dimensionless form by the maximum bubble radius (R_{TB}). For small values of Eu , the Taylor bubble is characterised by convex tails relatively to the liquid phase. As the Eötvös number increases, the tail starts to flatten, until the concavity is shifted. Regarding the Morton number of 4.72×10^{-5} , this transition should happen at an Eu around 30. From this point forward, the concave shape gets more pronounced, but the effect of Eu becomes residual near 150–200. Later on, the concavity transition for the remaining values of M under study will be addressed and compared to the corresponding values of the minimum Eu necessary to achieve wake formation.

The evolution just described is perfectly corroborated by the graph of the right side of Fig. 16, where the behaviour of the curvature radius of the bubble bottom with Eu is presented. These values were estimated by a similar procedure to the one previously applied to obtain the frontal radius. However, the small arcs of circle that approximately define the shape of the bubble tail had to respect two conditions:

- Radial coordinates lower than $0.7R_{TB}$.
- Axial coordinate distanced from the bubble tail less than $0.5R_{TB}$.

The stabilization length of the liquid flow field below the bubble tail (L_{min}), together with Z' , are features defined to highlight the influence of the Taylor bubble in its surroundings, which is particularly relevant for coalescence phenomena in continuous slug flow. For the majority of the flow conditions, this interference is much more pronounced below the bubble tail, where the stabilization lengths can reach several column diameters.

In Fig. 17, the simulation results obtained for the dimensionless stabilization length below the bubble tail (L_{min}/D) are illustrated. For a question of coherence, the criterion applied for estimating Z'/D was also adopted in the quantification of L_{min} (region where the normalised axial velocity, in the column centreline, and for a FFR, presents an absolute value higher than 1%).

From the observation of Fig. 17, it is clear that the numerical results of L_{min}/D are lacking of an uniform dependence on Eu , throughout the entire range of Morton and Eötvös numbers under study. This behaviour led to a division of the results into the three main regions pointed out in Fig. 17. For low Eu , corresponding to region (A), the dimensionless stabilization length is approximately constant and equal to 0.484. In region (B), for values of M within 1.64×10^{-2} and 104 and $Eu > 30$, the numerical results of L_{min}/D are linearly dependent on Eu , and a global equation was fitted to these results, valid only in the referred range:

$$L_{min}/D = 0.484 + 2.658 \times 10^{-3} \cdot M^{-0.336} (Eu - 30) \quad (10)$$

Eq. (10) reproduces almost perfectly the corresponding numerical data, with an average deviation of 2.7%, which is visually sustained by the proximity of the solid curves from the simulation points shown in Fig. 17.

When the Morton number decreases to 4.72×10^{-5} , the numerical L_{min}/D seems to change their dependence on Eu from linear to

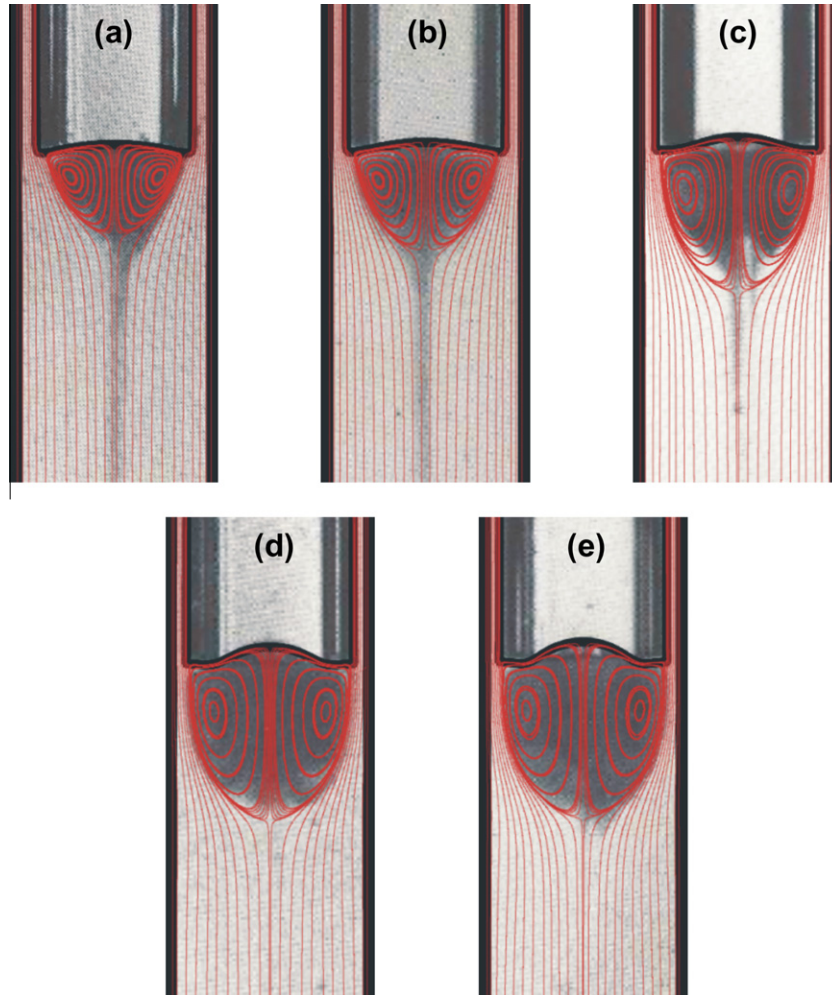


Fig. 15. Comparison between numerical and experimental (Campos and Guedes de Carvalho, 1988a) Taylor bubble wakes for conditions: (a) $N_f = 176$; (b) $N_f = 205$; (c) $N_f = 325$; (d) $N_f = 437$; and (e) $N_f = 483$.

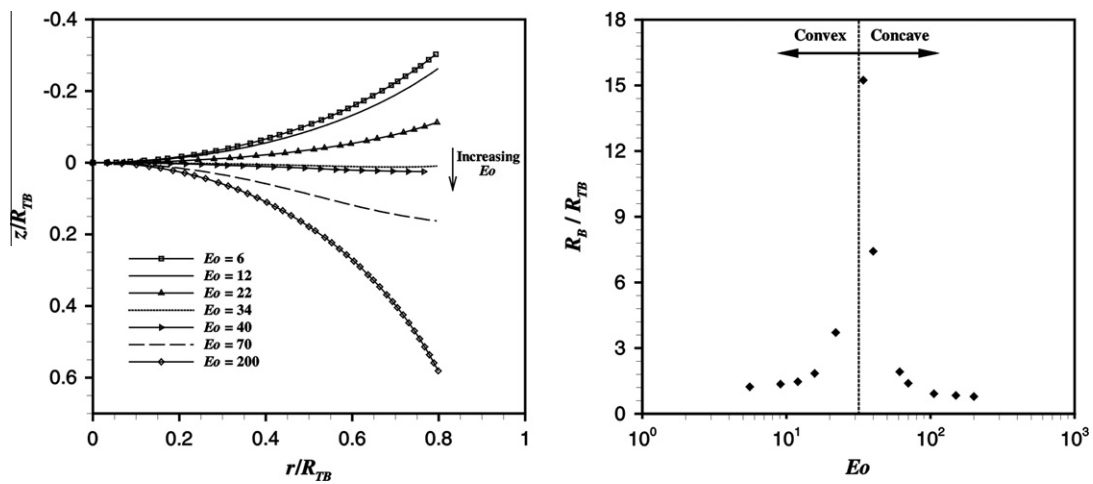


Fig. 16. Influence of Eo on the shape of the bubble tail for a M of 4.72×10^{-5} (graph on the left). The coordinates are presented in dimensionless form, using R_{TB} , and the origin of the axial coordinate is placed at the intersection between the column centreline and the bubble bottom. On the right side, the dimensionless bottom radius (R_B/R_{TB}) as a function of Eo , in logarithmic scale, is presented for the same Morton number. The dotted line indicates where the corresponding concavity transition occurs.

logarithmic, when this dimensionless number remains within the interval of 20–70 – region (C) of Fig. 17. For this particular region, the mentioned functionality can be expressed as:

$$L_{\min}/D = 2.683 \cdot \ln(Eo) - 7.541 \quad (11)$$

A fourth region was detached in Fig. 17 by a circle, including three numerical points, which occurs for M of 4.72×10^{-5} and when Eo exceeds approximately 70. This combination of Morton and Eötvös numbers implies an N_f around 300–400. The necessity

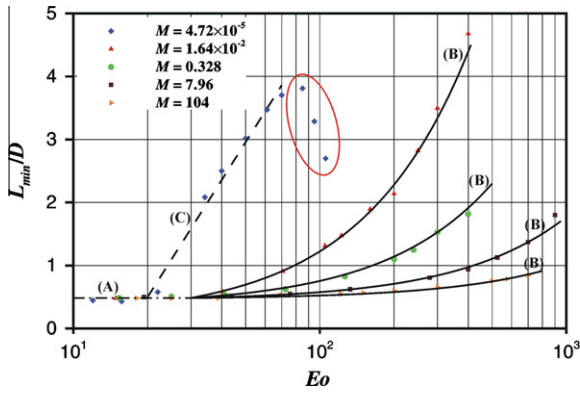


Fig. 17. Dependency of the dimensionless stabilization length below the bubble tail (L_{\min}/D) on Eo , for a set of five Morton numbers. The solid curves (B) represent fitted equations to the numerical data (solid points) in the range of $1.64 \times 10^{-2} < M < 104$ and $Eo > 30$. The dashed line (C) results from a fitted equation to estimate L_{\min}/D , for M of 4.72×10^{-5} , and Eo between 20 and 70. The dashed and dotted line (A) denotes a region where L_{\min}/D is constant (around 0.484) for low values of Eo .

to underline this region emerges from an abrupt change in the L_{\min}/D tendency with Eo , for this Morton number. In these cases, a more careful analysis was made separately to understand the causes of this change of behaviour. With that goal in mind, Fig. 18 was built by compiling the velocity vectors, in a fixed frame of reference (FFR), for some axial coordinate iso-surfaces, near the end and below the wake region, regarding two different conditions: the last numerical point inside the validity of Eq. (11), and the other one inside the circled region.

If the trend of Eq. (11) was to be followed by the systems spotlighted in Fig. 18, the liquid stabilization length should increase when advancing from Eo of 70–106. However, it was observed the opposite, and the main reason is offered by the differences on the evolution of the velocity fields shown in Fig. 18. Facing the question from the perspective of understanding what changed to fulfil the criterion used to estimate L_{\min} (u_z in the column centreline deviated less than 1% from u_z faraway from the Taylor bubble), it can be verified that, although for Eo of 106, the u_z (in FFR) close to the symmetry axis starts for z/D around 1 with higher values (in the upward direction), this intensity is attenuated much faster when comparing to the case of Eo of 70. Under the applied methodology used, this obviously leads to a smaller value of L_{\min}

for an Eötvös number of 106. The more abrupt velocity attenuation near the centreline, observed for this case, can find its motives embedded in the analysis of three different radial regions in each axial iso-surface: close to the symmetry axis, the liquid is moving upwards, followed by a part of the column cross-section where the liquid is descending (a result of the expansion of the liquid film somewhere above), and finally, close to the wall, the liquid movement is again upwards. The presence of the last upward movement of liquid, for each axial iso-surface, is a sign of an instantaneous recirculation zone, through the eyes of a fixed observer, affecting different liquid elements as the bubble moves upwards (unlike the recirculation inside the wake that consists of permanent liquid elements throughout the bubble path from the bottom to the top of the column). In other words, if an instantaneous photo is taken to the rising bubble and its surroundings, the recirculation zone will be detected in a region near the wall and below the tail that can be identified in the velocity vectors field (in FFR). If a new photo is taken moments later, with the bubble in a higher position inside the tube, the same kind of recirculation zone will be occurring at a similar distance from the bubble tail, but now affecting different fluid elements.

Lu and Prosperetti (2009) displayed streamlines for a system defined by $M = 1.8 \times 10^{-8}$ and $Eo = 60$ that seem to indicate the presence of a similar kind of recirculation zone near the tube wall. Nevertheless, the authors didn't checked or offered any particular attention to this kind of phenomenon in their work. Quan (2011) also reported a side vortex near the tube wall, for a downward co-current system, characterised by N_f of 22 and a liquid phase with viscosity of 1 Pa·s. However, the flow conditions and the nature of this vortex are quite different from what is discussed above, and so, any meaningful comparison can be done.

Returning to the relative dimensions of the radial regions previously identified, for the systems pointed out in Fig. 18, it is clear that the upward liquid movement, close to the wall, is more intense as it also propagates deeper in the axial and radial direction, for the case with higher Eo . This leads to an instantaneous recirculation zone much more extended. Even more relevant than that, it also decreases the need for high magnitudes in the upward axial velocity, near the column centreline, to compensate the movement of the descendent liquid in the intermediate radial region, and though respect the liquid continuity equation – in FFR the average liquid flow rate in each cross-section of the column must be zero. This decrease produces shorter stabilization zones as it is visible in Fig. 18.

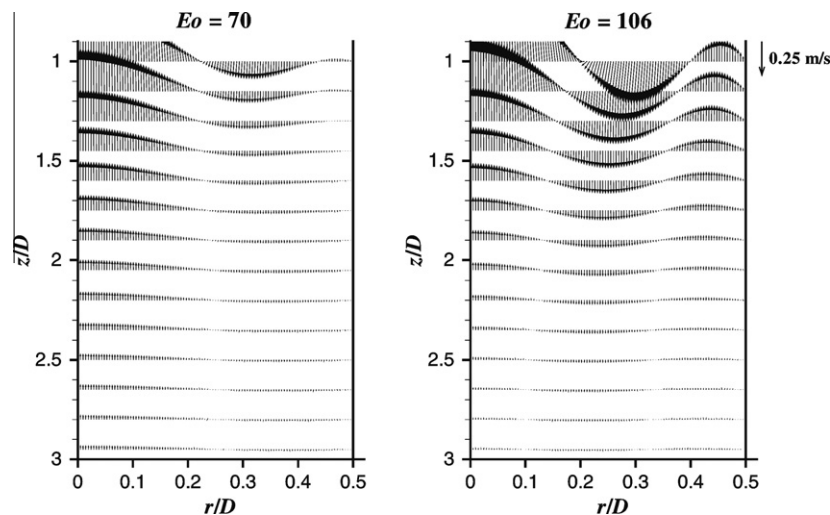


Fig. 18. Velocity vectors, in a FFR, for axial iso-surfaces close and below the end of the wake region, corresponding to two different systems with Morton number of 4.72×10^{-5} : Eo of 70 ($N_f = 292$) and 106 ($N_f = 397$). The reference position for the axial coordinate is the rear end bubble interface in centreline of the column.

It is important to add that, regarding the case of Eo of 106, the simulation was repeated for a larger domain (16.5 diameters long instead of the original 11 diameters) with the purpose of inferring if the outflow boundary has any influence on the flow behaviour previously described. The results were similar, which confirms that the domain reported is large enough and the bubble tail is sufficiently distanced from the outlet boundary.

Regarding the characterisation of the wake structure itself, this study included the numerical determination of size features – length (L_w) and volume (V_w) – and the position of the vortex centre (Z_V and R_V). The simulation results obtained for these features will be sequentially shown below, in graphical form, as a function of Eo and for a set of five different Morton numbers. Due to the smaller number of available points for these graphs, when compared to other features previously presented, at this stage it is important to remind that the formation of a wake does not always occur. Actually, a liquid recirculation zone, adjacent to the bubble tail, only develops for certain system conditions, that can be defined by different combinations of Eötvös and Morton numbers. A map that indicates the presence of wake depending upon the corresponding pair Eo and M , is also addressed later on.

For each wake feature under study, an equation was fitted with some functionality on Eo and M , and only valid within the applied ranges of these dimensionless numbers. Although a physical significance is absent on the referred equations, their purpose is to provide the reader a simple way to obtain an acceptable preliminary wake characterisation, without having to perform any experiment or numerical simulation.

In Fig. 19, the simulation results of the dimensionless wake length (L_w/D) are shown together with curves representing an equation fitted to these numerical points. As it was expected, there are two general conclusions that stand out: when M decreases, the minimum Eötvös number necessary to obtain a well-defined wake is smaller; when Eo is constant, decreasing the Morton number leads to bigger wakes. For L_w/D , the fitted equation is expressed by:

$$\frac{L_w}{D} = \frac{1}{4} \cdot [0.555 - 7.793 \times 10^{-3} \ln(M)] \cdot \ln\left(\frac{Eo^3}{M}\right) - 2.133 + 8.046 \times 10^{-2} \ln(M) \quad (12)$$

Looking at Fig. 19, it is fair to agree that the trend of Eq. (12) is relatively close to the one exposed by the simulation results of L_w/D . In fact, on the majority of the studied range of Eo and M , the deviations between the numerical L_w/D and the values estimated by Eq. (12) are very reasonable (absolute value below 15%). The exceptions encountered regard the system with the smaller wake

simulated for M of 4.72×10^{-5} (and $Eo = 34$) and three cases for the higher Morton numbers (7.96 and 104), where the relative errors stood between 23% and 43%.

Similarly to what was made for L_w/D , the numerical results of the dimensionless wake volume (V_w/D^3) and the corresponding fitted curves are compiled in Fig. 20. These results also reinforce the two general conclusions pointed out in the discussion of Fig. 19.

Comparing the simulation results of V_w/D^3 and L_w/D , it was observed that the relation between these features is very well defined by the following parabolic function:

$$\frac{V_w}{D^3} = 1.365 \times 10^{-1} \cdot \left(\frac{L_w}{D}\right)^2 + 2.176 \times 10^{-1} \cdot \left(\frac{L_w}{D}\right) - 2.919 \times 10^{-2} \quad (13)$$

The curves presented in Fig. 20 were built with the help of Eq. (13), that allows to define an implicit dependency of V_w/D^3 on Eo and M . Likewise the results of the wake length, in Fig. 20 is visible an acceptable agreement between the numerical V_w/D^3 and the prediction curves. This agreement seems to be weaker when the wakes are very small ($V_w/D^3 < 0.02$) and for large Eötvös numbers ($Eo > 700$). The deviations between the numerical V_w/D^3 and the estimations made by Eq. (13) are a little higher, when compared to the corresponding values regarding L_w/D . However, for the main part of the Eo and M ranges under consideration, the absolute value of these deviations are below 25%, which means that a reliable estimation of the wake size can be obtained combining Eqs. (12) and (13).

The methodology used to determine the numerical L_w/D and V_w/D^3 is supported on the assumption that the wake region is delimited by the bubble bottom and by the streamline that passes through the column centreline, in a region where the liquid flow is undisturbed by the Taylor bubble. After performing this delimitation, the corresponding volume can be obtained in the Ansys FLUENT (Release 12.0.1), with the help of proper customised field functions. Knowing the axial position of the upper and lower limits of the wake region, placed in the column centreline, the corresponding length can be easily calculated as the difference between these two axial coordinates.

To test the reliability of Eqs. (12) and (13), in Fig. 21 are compared experimental results of L_w/D and V_w/D^3 reported by Campos and Guedes de Carvalho (1988a), for the same gas–liquid systems addressed in Fig. 15, with the corresponding predictions calculated by the referred equations. These five systems have similar Eötvös number ($Eo \approx 62$) and M varying in the interval of 2.69×10^{-4} – 4.28×10^{-6} .

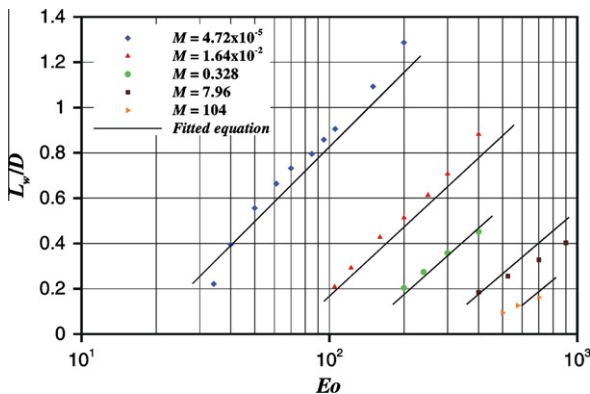


Fig. 19. Dimensionless wake length (L_w/D) as a function of the Eötvös number, in logarithmic scale, for a set of five Morton numbers. The points represent numerical results, and the solid lines were defined by an equation fitted to the same points.

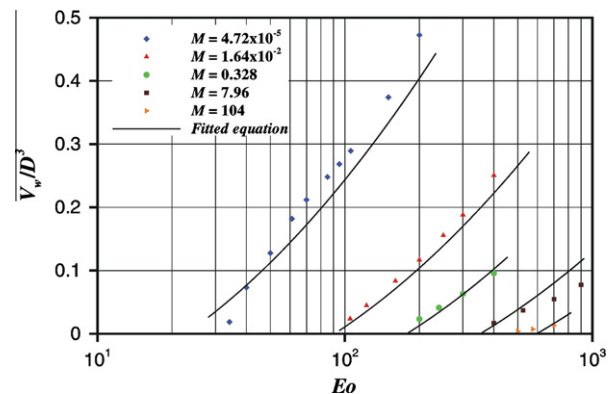


Fig. 20. Dimensionless wake volume (V_w/D^3) as a function of Eo , in logarithmic scale, for a set of five Morton numbers. The points are the numerical results, and the solid lines were defined by the combination of Eqs. (12) and (13).

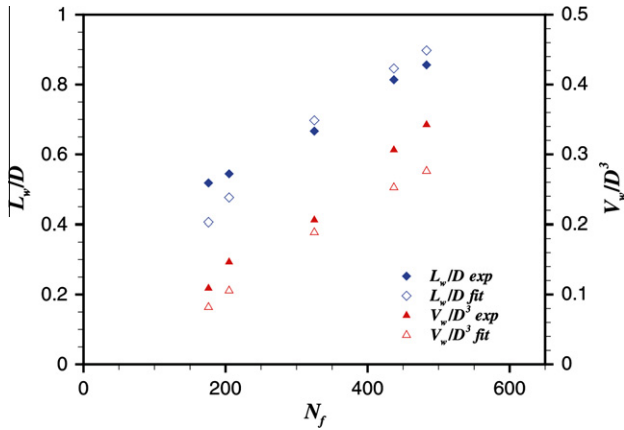


Fig. 21. Dimensionless wake length and volume (L_w/D and V_w/D^3) as a function of the inverse viscosity number (N_f), for a set of five different systems. The filled points represent the experimental data (Campos and Guedes de Carvalho, 1988a), and the empty ones were determined by Eqs. (12) and (13).

Performing a simple observation of Fig. 21, it can be concluded that the predictions made by the fitted equations have the same order of magnitude of the experimental data. Quantifying the previous affirmation, the estimations of L_w/D and V_w/D^3 have absolute deviations in the range of 4 to 28%, when compared to the corresponding experimental values. This fact is another proof that Eqs. (12) and (13) can produce quite reliable values for the wake length and volume, within the range of M under study. Since three of the five systems characterised in Fig. 21 have a Morton number below 4.72×10^{-5} , it also seems not too erroneous to further expand the M applicability range, by decreasing the original lower limit to the order of 10^{-6} .

Numerical results of the dimensionless axial (Z_v/D) and radial (R_v/D) coordinates of the vortex centre are presented in Fig. 22. These values were taken directly from the streamline maps built with the help of post-processing software. The reference of Z_v is the interface of the bubble tail in the column axis. Maintaining the kind of approach used on the wake size features, for each of the referred vortex centre coordinates, the simulation points were fitted to a proper function, taken Eo and M as independent variables. The obtained functions are expressed by:

$$\frac{Z_v}{D} = \frac{1}{4} \cdot [0.237 - 7.576 \times 10^{-3} \ln(M)] \cdot \ln\left(\frac{Eo^3}{M}\right) - 0.917 + 5.748 \times 10^{-2} \ln(M) \quad (14)$$

$$\frac{R_v}{D} = 0.291 - \frac{4.815}{\left(\frac{Eo^3}{M}\right)^{1/4} - 21.616 \cdot M^{-0.186}} \quad (15)$$

For the case of R_v/D , the fitted equation was forced to include a plateau of 0.291, equal to the maximum value of the simulation data. The curves resulting from the application of Eqs. (14) and (15) to the Morton numbers under the scope are also shown in Fig. 22. From the observation of this illustration, it can be inferred that Z_v/D has a similar behaviour as the one revealed by L_w/D . For that reason, Eqs. (12) and (14) have the same kind of functionality on Eo and M , only differing in the fitting parameters. Although for three simulated systems the estimations made by Eq. (14) are distant around 30–40% from the corresponding numerical data, the global ability of this equation to predict Z_v/D seems satisfactory, since the average of the absolute deviations between the predicted values and the numerical Z_v/D is 14.6%. Regarding the graph placed at the bottom of Fig. 22, it denotes almost a perfect match between the simulation values of R_v/D and the curves produced by Eq. (15).

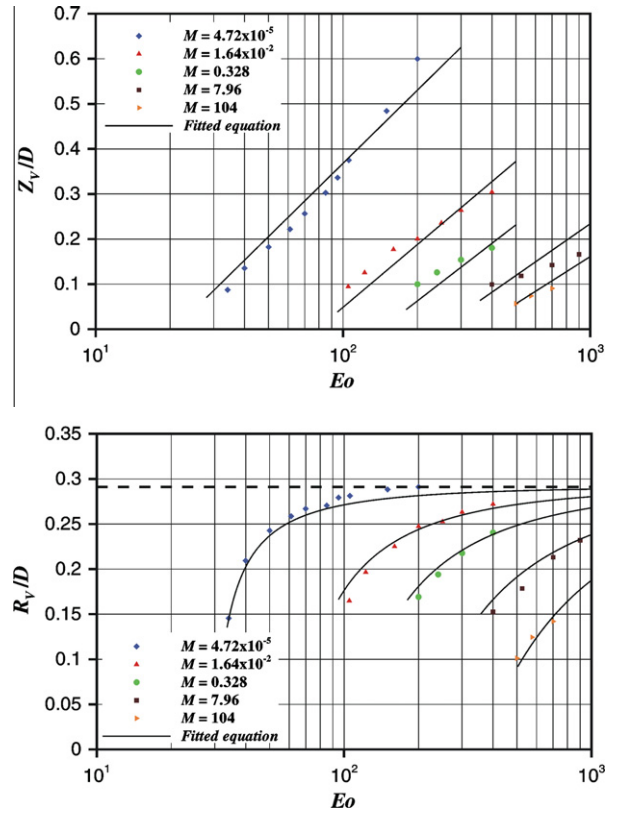


Fig. 22. Dimensionless axial (Z_v/D) and radial (R_v/D) coordinates of the vortex centre as a function of the Eötvös number, in logarithmic scale, for a set of five Morton numbers. The points represent the simulation data, and the solid curves result from the application of the fitted equations. For the radial coordinate (bottom graph) a dashed line is also placed to identify the plateau of the corresponding equation.

In addition to this visual conclusion, it should be said that the estimations do not exceed a 10% absolute deviation from the numerical R_v/D .

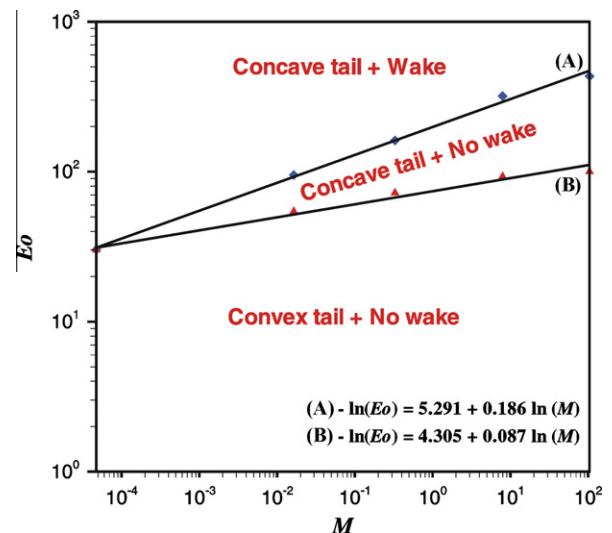


Fig. 23. Map indicative of the wake presence and the type of bubble tail concavity as a function of the Eötvös and Morton numbers, in logarithmic scale. The points are the numerical results, and the solid lines are the transitions curves estimated for the wake formation (A) and the bubble tail concavity (B).

Analysing the large spectrum of numerical data collected within this work, it was possible to condensate in a general map the information necessary to easily suggest when a wake region is formed (or not) and what kind of bubble tail is present, with the only requirement being the previous knowledge of the Eötvös and Morton numbers. To build this map, the first step was to define the transition curve between the systems with existence and absence of a wake region in their flow structure. With that goal in mind, for each Morton number under study, it was estimated the value of Eo for which the wake volume becomes zero, by performing separate extrapolations from the trend exhibited in the five available sets of numerical V_w/D^3 vs. Eo . It is important to mention that these estimations were not supported on the unique function defined by Eq. (13), since its inherent inaccuracy increases when dealing with wakes tending to zero volume. Based on the five collected pairs of Eo and M , the referred transition curve exhibits a linear relation between the logarithms of these two dimensionless number. Following a similar procedure to determine a transition curve for the concavity of the bubble tail, between convex to concave shape, it was also obtained a straight line relating the logarithms of Eo and M . The set of five numerical points related to this transition curve was obtained by interpolation, for each M , between the two consecutive Eo where it was verified an inflection of the tail curvature. Gathering all the information in the same graph, the final result is the pursued map shown in Fig. 23. The validity of this map is only circumscribed for Morton numbers in the range of 4.72×10^{-5} to 104.

4. Conclusions

A detailed and careful numerical study about the rising of Taylor bubbles through stagnant columns of Newtonian liquids is reported. The numerical method was supported on the VOF methodology implemented in the commercial code Ansys FLUENT (Release 12.0.1). All features proposed to characterise the hydrodynamics of this gas–liquid flow pattern were successfully determined from the gathered simulation data. The large amount of numerical results obtained was favourably compared with predictions made with some correlations and theoretical equations or, for some features, served as the basis to build our own predictive equations.

The numerical results were approached throughout this paper as a function of Eo and M or, in alternative, combining these two dimensionless numbers into N_f , and the analysis of the referred data was divided into four main parts (Taylor bubble velocity; flow around the bubble nose; liquid film; and wake region).

Regarding the Taylor bubble velocity, the simulations produced data within a 10% deviation from estimations made with the well-known correlation of Viana et al. (2003).

In the flow around the bubble nose, the first feature analysed was the frontal radius, where it was observed a small spread of numerical results around a mean value of $0.794R_{TB}$, which is not far from the frontal radius of $0.75R_{TB}$ suggested by Brown (1965). The dimensionless liquid flow stabilization length ahead of the bubble nose was found to be almost independent of M and N_f , and approximately equal to 0.483, when the inverse viscosity number is lower than 40. For higher values of N_f , this length showed a linear dependence with the natural logarithm of N_f .

Likewise it was observed for Z'/D , the results of the dimensionless film developing length were divided into a constant region up to an N_f around 90, with a value of 1.036, and a region of linear behaviour with N_f , for higher values of the inverse viscosity number.

The numerical results of the dimensionless stabilized liquid film thickness – δ/D – and wall shear stress – $\tau_w/(\rho_l g D)$ – were plotted together with curves obtained with the combination of the corre-

lation of Viana et al. (2003) and the theory proposed by Brown (1965), and the proximity between them is noteworthy.

Below the bubble tail, the simulation results of the studied features (wake length and volume, coordinates of the vortex centre and the minimum stabilization length) exhibit apparent consistent behaviours, and led to the presentation of predictive equations for each one of them, covering a wide range of Eo and M .

Finally, the information gathered throughout the analysis of the wake region allowed to build a map that, together with the knowledge of Eo and M , easily suggests the existence or absence of a wake structure and the type of concavity of the bubble rear.

Acknowledgments

The authors gratefully acknowledge the financial support from the Foundation for Science and Technology (FCT) through the project PTDC/EQU-FTT/69068/2006 and Grant SFRH/BPD/64148/2009. POCTI (FEDER) also supported this work via CEFT.

References

- Angeli, P., Gavrilidis, A., 2008. Hydrodynamics of Taylor flow in small channels: a review. *Proc. Inst. Mech. Eng. Part C J. Mech. Eng. Sci.* 222, 737–751.
- Brackbill, J.U., Kothe, D.B., Zemach, C., 1992. A continuum method for modeling surface tension. *J. Comput. Phys.* 100, 335–354.
- Branger, A.B., Lambertsen, C.J., Eckmann, D.M., 2001. Cerebral gas embolism absorption during hyperbaric therapy: theory. *J. Appl. Physiol.* 90, 593–600.
- Brown, R.A.S., 1965. The mechanism of large bubbles in tubes. I. Bubble velocities in stagnant liquids. *Can. J. Chem. Eng.* 43, 217–223.
- Bugg, J.D., Mack, K., Rezkallah, K.S., 1998. A numerical model of Taylor bubbles rising through stagnant liquids in vertical tubes. *Int. J. Multiphase Flow* 24, 271–281.
- Campos, J.B.L.M., Guedes de Carvalho, J.R.F., 1988a. An experimental study of the wake of gas slugs rising in liquids. *J. Fluid Mech.* 196, 27–37.
- Campos, J.B.L.M., Guedes de Carvalho, J.R.F., 1988b. Mixing induced by air slugs rising in narrow columns of water. *Chem. Eng. Sci.* 43, 1569–1582.
- Chung, E.M.L., Hague, J.P., Evans, D.H., 2007. Revealing the mechanisms underlying embolic stroke using computational modelling. *Phys. Med. Biol.* 52, 7153–7166.
- Clanet, C., Héraud, P., Searby, G., 2004. On the motion of bubbles in vertical tubes of arbitrary cross-sections: some complements to the Dumitrescu–Taylor problem. *J. Fluid Mech.* 519, 359–376.
- Clarke, A., Issa, R., 1997. A numerical model of slug flow in vertical tubes. *Comput. Fluids* 26, 395–415.
- Davies, R.M., Taylor, G., 1950. The mechanics of large bubble rising through extended liquids and through liquids in tubes. *Proc. R. Soc. Lond. A* 200, 375–390.
- Dumitrescu, D.T., 1943. Strömung an einer Luftblase im Senkrechten Rohr. *Z. Angew. Math. Mech.* 23, 139–149.
- Fabre, J., Liné, A., 1992. Modelling of two-phase slug flow. *Annu. Rev. Fluid Mech.* 24, 21–46.
- Fulford, G.D., 1964. The flow of liquids in thin films. *Adv. Chem. Eng.* 5, 151–236.
- Funada, T., Joseph, D.D., Maehara, T., Yamashita, S., 2005. Ellipsoidal model of the rise of a Taylor bubble in a round tube. *Int. J. Multiphase Flow* 31, 473–491.
- Ghosh, R., Cui, Z.F., 1999. Mass transfer in gas-sparged ultrafiltration: upward slug flow in tubular membranes. *J. Membr. Sci.* 162, 91–102.
- Hirt, C.W., Nichols, B.D., 1981. Volume of fluid (VOF) method for the dynamics of free boundaries. *J. Comput. Phys.* 39, 201–225.
- Kang, C.-W., Quan, S., Lou, J., 2010. Numerical study of a Taylor bubble rising in stagnant liquids. *Phys. Rev. E* 81, 066308.
- Kawaji, M., DeJesus, J.M., Tudose, G., 1997. Investigation of flow structures in vertical slug flow. *Nucl. Eng. Des.* 175, 37–48.
- Liberzon, D., Shemer, L., Barnea, D., 2006. Upward-propagating capillary waves on the surface of short Taylor bubbles. *Phys. Fluids* 18, 048103.
- Lu, X., Prosperetti, A., 2009. A numerical study of Taylor bubbles. *Ind. Eng. Chem. Res.* 48, 242–252.
- Mercier, M., Fonade, C., Lafforgue-Delorme, C., 1997. How slug flow can enhance the ultrafiltration flux in mineral tubular membranes. *J. Membr. Sci.* 128, 103–113.
- Nešić, S., 2007. Key issues related to modelling of internal corrosion of oil and gas pipelines – a review. *Corros. Sci.* 49, 4308–4338.
- Nogueira, S., Sousa, R.G., Pinto, A.M.F.R., Riethmüller, M.L., Campos, J.B.L.M., 2003. Simultaneous PIV and pulsed shadow technique in slug flow: a solution for optical problems. *Exp. Fluids* 35, 598–609.
- Nogueira, S., Riethmüller, M.L., Campos, J.B.L.M., Pinto, A.M.F.R., 2006a. Flow in the nose region and annular film around a Taylor bubble rising through vertical columns of stagnant and flowing Newtonian liquids. *Chem. Eng. Sci.* 61, 845–857.
- Nogueira, S., Riethmüller, M.L., Campos, J.B.L.M., Pinto, A.M.F.R., 2006b. Flow patterns in the wake of a Taylor bubble rising through vertical columns of

- stagnant and flowing Newtonian liquids: an experimental study. *Chem. Eng. Sci.* 61, 7199–7212.
- Pangarkar, K., Schildhauer, T.J., van Ommen, J.R., Nijenhuis, J., Kapteijn, F., Moulijn, J.A., 2008. Structured packing for multiphase catalytic reactors. *Ind. Eng. Chem. Res.* 47, 3720–3751.
- Polonsky, S., Shemer, L., Barnea, D., 1999. The relation between the Taylor bubble motion and the velocity field ahead of it. *Int. J. Multiphase Flow* 25, 957–975.
- Quan, S., 2011. Co-current flow effects on a rising Taylor bubble. *Int. J. Multiphase Flow* 37, 888–897.
- Shemer, L., Gulitski, A., Barnea, D., 2007. On the turbulent structure in the wake of Taylor bubbles rising in vertical pipes. *Phys. Fluids* 19, 035108.
- Taha, T., Cui, Z.F., 2002. CFD modelling of gas-sparged ultrafiltration in tubular membranes. *J. Membr. Sci.* 210, 13–27.
- Taha, T., Cui, Z.F., 2006. CFD modelling of slug flow in vertical tubes. *Chem. Eng. Sci.* 61, 676–687.
- van Hout, R., Gulitski, A., Barnea, D., Shemer, L., 2002. Experimental investigation of the velocity field induced by a Taylor bubble rising in stagnant water. *Int. J. Multiphase Flow* 28, 579–596.
- Viana, F., Pardo, R., Yáñez, R., Trallero, J.L., Joseph, D.D., 2003. Universal correlation for the rise velocity of long gas bubbles in round pipes. *J. Fluid Mech.* 494, 379–398.
- Villarreal, J., Laverde, D., Fuentes, C., 2006. Carbon–steel corrosion in multiphase slug flow and CO₂. *Corros. Sci.* 48, 2363–2379.
- Wallis, G.B., 1969. *One-Dimensional Two-Phase Flow*. McGraw Hill, New York.
- White, E.T., Beardmore, R.H., 1962. The velocity of rise of single cylindrical air bubbles through liquids contained in vertical tubes. *Chem. Eng. Sci.* 17, 351–361.
- Youngs, D.L., 1982. Time-dependent multi-material flow with large fluid distortion. In: Morton, K.W., Baibnes, M.J. (Eds.), *Numerical Methods for Fluid Dynamics*. Academic Press, New York.